Astronomy & Astrophysics manuscript no.
(will be inserted by hand later)

A new sample of giant radio galaxies from the WENSS survey

I - Sample definition, selection effects and first results

A.P. Schoenmakers[1,2,3⋆], A.G. de Bruyn[3,4], H.J.A. Röttgering[2], and H. van der Laan[1]

[1] Astronomical Institute, Utrecht University, P.O. Box 80 000, 3508 TA Utrecht, The Netherlands
[2] Sterrewacht Leiden, Leiden University, P.O. Box 9513, 2300 RA Leiden, The Netherlands
[3] ASTRON, P.O. Box 2, 7990 AA Dwingeloo, The Netherlands
[4] Kapteyn Astronomical Institute, University of Groningen, P.O. Box 800, 9700 AV Groningen, The Netherlands

Received ; accepted

Abstract. We have used the Westerbork Northern Sky Survey (WENSS) to define a sample of 47 low redshift ($z \lesssim 0.4$) giant radio galaxies. This is the largest sample yet of such radio sources originating from a single survey. We present radio maps of the newly discovered giants and optical images and spectra of their host galaxies. We present some of their properties and discuss the selection effects. We investigate the distribution of the sources in the radio power – linear size ($P - D$) diagram, and how these parameters relate to the redshifts of the sources in our sample. We find a strong drop in the number of sources with a linear size above 2 Mpc. We argue that this is not a result of selection effects, but that it indicates either a strong luminosity evolution of radio sources of such a size, or that a large fraction of radio sources 'switch off' before they are able to grow to a size of 2 Mpc.

Key words. Galaxies: active – Intergalactic medium – Galaxies: jets – Radio continuum: galaxies

1. Introduction

The central activity in a fraction of Active Galactic Nuclei (AGN) is capable of producing relativistic outflows of matter, the so-called 'jets', for a prolonged period of time, possibly up to a few 10^8 yr. These jets, when powerful enough, inflate a cocoon (e.g. Scheuer 1974, Falle 1991) which expands first in the Interstellar Medium (ISM) and later in the Intergalactic Medium (IGM) of the host galaxy. The evolution of such cocoons is traced by the radio lobes, which in themselves are only a (albeit important) 'side effect' caused by the presence of magnetic fields in the cocoon.

The giant radio galaxies (GRGs) are those radio sources whose lobes span a (projected) distance of above 1 Mpc[1]. As such, GRGs must represent a late phase in the evolution of radio sources. Models of radio source evolution (e.g. Kaiser et al. 1997 and Blundell et al. 1999) predict the radio power and linear size evolution of powerful radio sources with time. According to these models, GRGs must be extremely old (i.e. typically older than 10^8 yr) and probably also located in underdense environments, as compared to smaller radio sources of comparable radio power (e.g. Kaiser & Alexander 1999).

Multi-frequency radio observations (Mack et al. 1998) have shown that spectral ages of GRGs are of the same order as expected from source evolution models. It is, however, not clear at all whether *spectral* ages are representative of the *dynamical* ages (e.g. Parma et al. 1999). This questions the validity of radio-based determinations of the properties of the environments of these sources. Still, constraints on the environments of GRGs are of high importance since the radio lobes of these sources penetrate deeply into the intergalactic medium. It is almost impossible to find the properties of this medium, otherwise than from studies of such radio lobes (e.g. Subrahmanyan & Saripalli 1993).

A major problem for such studies is that currently known GRGs have not been uniformly selected. The difficulties encountered while selecting extended radio sources has been demonstrated by Saunders et al. (1987), who searched for GRGs in a small region of the 151-MHz 6C survey. The 6C survey, with only 30 mJy beam^{-1} RMS-noise and a beamsize of $4.2' \times 4.2'$ cosec δ FWHM (with δ the declination) has an excellent sensitivity to large, faint objects. However, using higher resolution observations they found that only at integrated flux densities above 5 Jy has a radio source larger than $5'$ a good chance

Send offprint requests to: A.P. Schoenmakers (Schoenmakers@astron.nl)
⋆ *Present address:* ASTRON, P.O. Box 2, 7990 AA Dwingeloo, The Netherlands

[1] We use $H_0 = 50$ km s^{-1} Mpc^{-1} and $q_0 = 0.5$ throughout this paper.

of being a genuine GRG in the 6C. At a flux density level of 1 Jy, Saunders et al. find that most of the sources which appear as large extended structures on the 6C survey maps are the result of confusion of physically unrelated sources. Their work demonstrates that 1) an efficient search for GRGs has to be done with sufficient angular resolution to minimize confusion problems and that 2) it should be done with a high sensitivity, also for large-scale structures (up to a few tens of arcmin) on the sky. The recently completed WENSS survey (Rengelink et al. 1997) meets both these demands.

In this paper we report of the selection of new giant radio sources from the WENSS. Subsequent papers will present additional radio observations (Schoenmakers et al. 2000b), a more detailed analysis of the spectroscopic data and a discussion of the evolution of GRGs (in preparation, but see Schoenmakers 1999a). In Sect. 2 we outline the selection technique and criteria. Section 2.5 presents the strategy we have adopted for finding the optical identifications, and Sect. 3 describes the spectroscopic observations of these identifications. In Sect. 4 we present the first results of the new sample of GRGs: Flux densities, linear sizes, redshifts, etc. A discussion of these results and on the sensitivity of the WENSS survey to extended radio sources is given in Sect. 5.

Throughout this paper, a spectral index α is defined according to the relation $S_\nu \propto \nu^\alpha$ between flux density S_ν at frequency ν, and the frequency ν.

2. Sample selection

2.1. The WENSS survey

The Westerbork Northern Sky Survey is a 325-MHz survey of the sky above +28° declination. About a quarter of this area has also been observed at a frequency of 609 MHz. The unique aspect of WENSS is that it is sensitive to spatial structures over 1 degree on the sky at 325 MHz. The limiting flux density to unresolved sources is about 15 mJy (5σ) and the FWHM of the beam is $54'' \times 54''\mathrm{cosec}\,\delta$, with δ the declination. A detailed description of the observing and data reduction techniques used can be found in Rengelink et al. (1997). The sky area above +74° declination has been observed with an increased total bandwidth, so that the limiting flux density to unresolved sources is about 10 mJy (5σ) in this sky area.

Using the Wieringa (1991) source counts at 325-MHz, the flux density at which the same amount of confusion in the WENSS as Saunders et al. (1987) encountered in the 6C survey can be calculated. For a typical radio source spectral index of -0.8, a similar amount of confusion can be expected in the WENSS at a flux density of ~ 400 mJy, which is almost seven times lower than that for the 6C survey. Similarly, it can be shown that confusion would dominate the selection sources only below 20 mJy in the WENSS survey, which is below its completeness limit of $\sim$ 30 mJy (Rengelink et al. 1997). This implies that we should be able to efficiently find GRGs in the WENSS down to relatively low flux density levels.

2.2. Selection criteria

In order for a source to be a candidate low redshift GRG, we have used the following criteria. A candidate GRG must have:

1. an angular size larger than 5 arcminute, and
2. a distance to the galactic plane of more than 12.5 degree.

The angular size lower limit of $5'$ is the size at which some basic morphlogical information of a source can still be obtained at all declinations the survey has covered. this corresponds to a physical size of ~ 750 kpc at $z = 0.1$, $\sim$1300 kpc at $z = 0.2$ and $\sim$1700 kpc at $z = 0.3$, and will therefore introduce a redshift-dependent linear size bias in the sample. To avoid high galactic extinction values and confusion by a large surface density of foreground stars, we have restricted ourselves to galactic latitudes above 12.5°. This results in a survey area of ~ 2.458 steradian ($\sim 8100^{\square}$).

Tab. 1 presents all previously discovered GRGs whose angular size and position on the sky agree with the above selection criteria. The majority of these are smaller than 2 Mpc in size. If their sizes are characteristic for the whole population of GRGs, we thus expect that the majority of selected sources will have a redshift below $\sim$0.35. Assuming that the host galaxies are not less luminous than those of the LRL sample of powerful radio sources (Laing et al. 1983) they should be identifiable on the Digitized POSS-I survey (DSS).

2.3. Selection method

Candidate radio sources were selected using a visual inspection of the WENSS radio maps. We preferred this method over possibly more objective, machine controlled selection methods because the complexity of the WENSS radio maps (i.e the high source surface density and the unavoidable presence of spurious artefacts such as low-level sidelobes of bright sources, etc.) and the wide variety in possible morphologies would make it very difficult to tune such an algorithm. Looking at the maps allows one to easily recognize low-level extended structures in a crowded field.

Above declination +74° we have initially selected our candidates using the earlier available NVSS survey maps (Condon et al. 1998), but we subsequently repeated the selection using the WENSS maps. We found that no WENSS selected candidates were omitted using the NVSS. On the contrary, we have identified two NVSS sources (B 1044+745 and B 0935+743) that we most likely would not have selected from the WENSS survey alone due to their faintness in the latter. We will elaborate on this when we discuss the selection effects (Sect. 5.1).

Table 1. List of all previously known GRGs (i.e. before 1998) in the area of the sky covered by the WENSS and fulfilling our selection criteria. Column 1 gives the name of the source in IAU-format; column 2 gives the more common name of the source, if available; column 3 and 4 give the coordinates of the host galaxy in B1950.0; column 5 and 6 give the redshift of the host galaxy and a reference to it; column 7 gives the projected linear size of the radio source in Mpc; column 8 designate the morphological type of the radio source, i.e. FRI or FRII or an intermediate type, FRI/II. If a 'B' is added, it means that the host galaxy is a broad-line object, a 'Q' means that it is a quasar. Column 9 gives a reference to radio maps in which the radio morphology can be studied. Columns 10 and 11 give the flux density at 325 MHz and the reference for this value.

(1) IAU Name	(2) Other name	(3) R.A. (B1950.0)	(4) Dec. (B1950.0)	(5) z	(6) Refs.	(7) Size [Mpc]	(8) Type FR	(9) Refs.	(10) S_{325} [Jy]	(11) Refs.
B 0050+402		00 50 45.1	40 11 10.0	0.1488	DJ95	1.5	II	V89	1.41 ± 0.04	WE
B 0055+300	NGC 315	00 55 05.6	30 04 56.8	0.0167	C75	1.7	I/II	W81	9.71 ± 0.18	M97
B 0104+321	3C 31	01 04 39.2	32 08 44.0	0.0169	S97	1.3	I	S83	13.67 ± 0.28	WE
B 0109+492	3C 35	01 09 04.1	49 12 40.1	0.06701	B72	1.1	II	B82	7.19 ± 0.15	WE
B 0136+396	4C 39.04	01 36 33.6	39 41 51.2	0.2107	S73	1.6	II	FB78,H79	4.75 ± 0.10	WE
B 0157+405	4C 40.09	01 57 22.4	40 34 34.2	0.0827	DJ95	1.9	I/II	V89	2.98 ± 0.08	WE
B 0309+411		03 09 44.8	41 08 48.7	0.134	B89	1.8	II-B	B89	1.38 ± 0.04	WE
B 0745+560	DA 240	07 45 46.1	56 01 56.2	0.0356	W74	2.0	II	S81	17.05 ± 0.35	M97
B 0821+695		08 21 01.9	69 30 25.8	0.538	L93	3.0	II	L93	0.63 ± 0.02	WE
B 0945+734	4C 73.08	09 45 09.9	73 28 22.2	0.0581	D70	1.5	II	J86	10.43 ± 0.21	WE
B 1003+351	3C 236	10 03 05.4	35 08 48.0	0.0989	S85	5.7	II	S80	13.13 ± 0.26	M97
B 1029+570	HB 13	10 29 48.2	57 00 45.8	0.045	S96	2.6	I	MA79	1.09 ± 0.04	WE
B 1209+745	4CT 74.17	12 09 36.0	74 35 45.5	0.107	M79	1.2	II	B81	2.06 ± 0.05	WE
B 1309+412		13 09 27.1	41 14 53.5	0.1103	D90	1.0	II	V89	1.61 ± 0.04	WE
B 1312+698	DA 340	13 12 22.1	69 53 10.0	0.1060	S87	1.3	II	S87	4.16 ± 0.09	WE
B 1358+305		13 58 29.3	30 33 47.7	0.206	P96	2.6	II	P96	1.84 ± 0.04	P96
B 1626+518		16 26 48.5	51 53 05.0	0.0547	G92	1.6	II-B	R96	1.62 ± 0.03	WE
B 1637+826	NGC 6251	16 37 57.0	82 38 18.6	0.023	W77	3.0	I/II	P84	11.55 ± 0.23	M97
B 2043+749	4C 74.26	20 43 13.0	74 57 08.7	0.104	R88	1.6	II-Q	R88	4.76 ± 0.10	WE

References: B72: Burbidge & Strittmattar 1972; B81: van Breugel & Willis 1981; B82: van Breugel & Jägers 1982; B89: de Bruyn 1989; C75: Colla et al. 1975; D70: Demoulin 1970; D90: Djorgovski et al. 1990; DJ95: Djorgovski et al. 1995; FB78: Fomalont & Bridle 1978; G92: de Grijp et al. 1992; H79: Hine 1979; J86: Jägers 1986; M79: Miley & Osterbrock 1979; MA79: Masson 1979; M96: Marcha et al. 1996; M97: Mack et al. 1997; P84: Perley, Bridle & Willis 1984; P96: Parma et al. 1996; R88: Riley et al. 1988; R96: Röttgering et al. 1996; S73: Sargent 1973; S80: Strom & Willis 1980; S81: Strom et al. 1981; S82: Saunders 1982; S83: Strom et al. 1983; S85: Spinrad et al. 1985; S86: Saripalli et al. 1986; S87: Saunders et al. 1987; S97: Simien & Prugniel 1997; V89: Vigotti et al. 1989; WE : WENSS (measured in the radio map); W74: Willis et al. 1974; W77: Wagett et al. 1977; W81: Willis et al. 1981.

2.4. Removing confused sources

The declination dependent beam size results in an unavoidable increase of confusion with decreasing declination. Only with higher angular resolution observations can we determine whether such sources are separate unrelated radio sources. We have used the following additional sources of radio data to achieve this:

First, where available, we have used the 612-MHz WENSS maps which have twice the resolution of the 325-MHz maps. Also the 1.4-GHz NVSS survey, which does not have a declination-dependent beam size and which covers almost the entire area of the WENSS survey, is highly usefull in this respect. Furthermore, we have used the much higher resolution (5.″4 FWHM) maps from the 1.4-GHz FIRST survey (Becker et al. 1995) where available. Also the FIRST survey has mapped a large fraction of the area observed by WENSS, notably the lower declination range away from the galactic plane. Finally, for candidates in areas of the sky where the FIRST survey was not (yet) available, we obtained short 1.4-GHz WSRT observations.

A consequence of the different methods used to eliminate confused sources is that the angular size of the objects are not well determined in all cases. There are two important factors which influence such estimates: First, for edge-brightened sources (FRII-type) high-resolution observations would be required for an accurate measurement, but we do not have these for all such sources and even the ones we have differ in quality and resolution. Second, for FR-I type sources the angular size measured on a map depends strongly on surface-brightness sensitivity. Therefore, sources may have been accidentally removed from the sample because of wrongly estimated sizes.

2.5. Identification of the host galaxies

We have used the digitized POSS-I survey (the 'Digitized Sky Survey', DSS) and, in a later stage, also the digitized POSS-II survey to identify the host galaxies of the selected radio sources. The magnitude limit of the red POSS-I plates is $\sim 20 - 20.5$; the POSS-II is somewhat more sensitive.

Adopting the Cousin R-band magnitude – redshift relation for the host galaxies of the radio sources in the LRL sample (Dingley 1990), we expect to be able to identify host galaxies out to $z \sim 0.5$ (note that the transmission curves of the Cousin R-band and the POSS-E band are much alike).

To identify the host galaxy of a radio source which extends over several arcminutes, a radio core position is often necessary. We have used the WENSS, NVSS, FIRST and our own WSRT radio observations to identify radio cores of the selected sources. For many sources we indeed find a compact central radio source coincident with an optical galaxy in the POSS-I and/or POSS-II.

We cannot rule out that for an individual source the so-found optical galaxy is an unrelated foreground galaxy, and that the actual host galaxy of the radio source is a much farther and fainter galaxy. However, for the sample as a whole, we believe this to be only a minor problem: It would make the radio sources even larger than they already are and the chance of such an occurrence is very small anyway.

For the source B 1918+516 the POSS-I plates did not show an obvious host galaxy candidate. Therefore, an optical CCD image has been made by P.N. Best using the LDSS imaging spectrograph on the 4.2-m WHT telescope on La Palma. This image (see Fig. A.28) reveals a faint galaxy, close to a relatively bright star. We believe this galaxy to be the host galaxy, due to its proximity to the radio core.

We cross-correlated the positions of the optical galaxies with the NASA Extragalactic Database (NED). In case an optical source with known redshift is found and the resulting size of the radio source is below 1 Mpc, we removed that source from our sample. We present the list of remaining (i.e. after removing sources identified as non-GRGs on basis of NED data) candidate GRG sources in Tab. A.1. We provide IAU-formatted source names, approximate coordinates of the radio sources, WENSS flux densities, approximate angular sizes and whether we are convinced this a genuine giant radio galaxy candidate on basis of its radio morphology. We remark that many of the WENSS selected sources were rejected after a look at the maps of these sources from the NVSS survey.

3. Optical spectroscopy

Optical spectra of a large fraction of possible host galaxy of the candidates have been obtained. In order to construct an as complete as possible flux-density limited sample from our candidates, we have tried to obtain spectra and redshifts for all candidate sources in Tab. A.1 with a 325-MHz flux density above 1 Jy [2].

In Tab. A.2 we present the log of the spectroscopic observations. On the 2.5-m INT telescope on La Palma we used the IDS-235 camera with the Ag-Red collimator and the R300V grating. The camera was equipped with a 1k×1k TEK chip. This setup results in a total wavelength coverage of ~ 3500Å and a pixel scale of ~ 3.2Å/pixel in the dispersion direction and $0\farcs74$/pixel in the spatial direction. Depending on the magnitude estimated redshift of the host galaxy candidate, the central wavelength of the spectrograph was set at either 5500, 6000 or 6500Å. The slit-width was held constant at $2''$. Only in the case of the source B 0809+454 we used a $3''$-wide slit because of uncertainties in the optical position at the time of observation. Flat-field observations were made at the beginning of each night by using the internal Tungsten lamp. Wavelength calibration was achieved by internal arc-lamp exposures (from CU-AR and CU-NE lamps) which were taken at the beginning of each night and immediately after each object exposure. For absolute flux calibration and to correct for the wavelength-dependent sensitivity of the instrument, several spectroscopical standard stars were observed each night, using a $5''$-wide slit.

The spectra have been reduced using the NOAO IRAF data reduction software. One dimensional spectra have been extracted using a $4''$-wide aperture centered on the peak of the spatial profile of the identification. The resulting spectra are shown in Figs. A.1-A.29. For each object exposure the wavelength calibration has been checked against several bright sky-lines in a non background-subtracted frame.

In addition to these observations, a spectrum of the source B 1450+333 was obtained on 8 July 1997 by P.N. Best, using the 4.2-m WHT on La Palma, equipped with the ISIS spectrograph. An optical CCD image and a spectrum of the source B 1543+845 were obtained by I.M. Gioia on 4 and 5 March 1998 using the HARIS imaging spectrograph on the 2.2-m University of Hawaii Telescope on Mauna Kea, Hawaii.

Table A.5 presents the measured redshifts and the spectral features used to determine these. The optical images and spectra of the observed host galaxies are presented in Figs. A.1–A.29. For the source B 1245+676 a

[2] From a recent paper by Lara et al. (2001), however, it was noted that three genuine candidate sources were missed after a first selection round from WENSS (B 1838+658, B 1919+741, B 0603+612). The source B 1838+658 has a redshift of 0.23 (NED) and is as such a GRG; for B 1919+741 the redshift is 0.194 and for B 0603+612 it is 0.227 (Lara et al. 2001). Also, the source B 1855+310 was not further observed. Further, high resolution observations by Lara et al. show that some sources, whose size was estimated to be less than $5'$ on basis of the WENSS maps, actually have angular sizes $\gtrsim 5'$ and should thus be included in our candidate sample. The implication of these findings is that the earlier made claim that we have observed a complete flux-density limited sample of GRGs (paper II, Schoenmakers et al. 2000b), must be recalled.

high-quality spectrum and the therefrom derived redshift had been published earlier by Marcha et al. (1996). We have therefore not observed the host galaxy of this radio source again. We have, however, reobserved the source B 1310+451 in order to obtain a higher quality spectrum of the host galaxy of this source.

Several other radio and optical properties of the observed candidates, and of the three sources that were found to be GRGs from available data in the NED (B 1144+352, B 1245+676 and B 1310+451) are given in Tab. A.3 and A.4.

4. First results

4.1. The number of GRGs

Of the 33 candidate sources which we have been able to identify spectroscopically, only three, and possibly five have projected linear sizes below 1 Mpc. These are B 0217+367, B 1709+465 and B 1911+479. The uncertain cases are the source B 0905+352, for which we do not have a well determined redshift yet and B 1736+375 which may consist of two unrelated radio sources. Together with the 19 known GRGs in the area of the WENSS which share our selection criteria, we have so far identified 47 GRGs. This is by far the largest sample of sources with a projected linear size above 1 Mpc selected from a single survey. We also mention the existence of the large, but highly incomplete sample of GRGs which has been compiled by Ishwara-Chandra & Saikia (1999) from the literature. Although of similar size, the sample presented in this paper is better suited for statistical investigations of the radio and optical properties of GRGs since it has been selected from a single survey and in a more uniform matter.

4.2. Distribution functions of the sample

4.2.1. Flux density distribution

Fig. 1a presents a histogram of the 325-MHz flux density distribution of the sample of 47 sources. The hatched bars indicate the flux density distribution of the sample of previously known GRGs. Not surprisingly, we find that all newly discovered GRGs have flux densities below 3 Jy, only; all ten GRGs with a 325-MHz flux density above this value had already been identified as such. For the area of the sky covered by WENSS, we can therefore agree with Riley (1989) who argued that no bright extended sources are missing from the LRL sample of bright radio sources ($S_{178} > 10.9$ Jy, Dec. $> +10°$, $|b| > 10°$). Furthermore, we have extended the range of flux densities at which low redshift GRGs are found to sub-Jy levels. The median flux density of the combined sample is 1.15 Jy, which is almost a factor of four below the median value of the sample of previously known GRGs (see Tab. 2).

4.2.2. Redshift distribution

The new sample of GRGs mostly contains GRGs at $z \lesssim 0.3$ (see Fig. 1b). The only exceptions are the sources 8C 0821+695 ($z = 0.538$; Lacy et al. 1993), B 0750+434 ($z = 0.347$) and B 0925+420 ($z = 0.365$). The redshift distribution peaks at $z \sim 0.1$. The decrease in the number of sources towards higher redshift is likely to be due to the lower angular size limit used in the selection of the sample. Further, only more powerful GRGs will be selected towards higher redshift, of which the space density is likely to be lower. The median redshift of the sample of new GRGs is 0.1404, which is higher than that of the old GRGs alone (0.099; see Tab. 2). Since the average flux density is lower this is not surprising. The median redshift of the combined sample is 0.1175 .

4.2.3. Linear size distribution

No source with a (projected) linear size exceeding that of the GRG 3C 236 has been found. This source is therefore still the largest known radio galaxy in the Universe. In Fig. 1c we have plotted the (projected) linear size distribution of our sample. The median values of the linear sizes of the old and new GRGs lie close together (see Tab. 2). The majority of sources have linear sizes between 1 and 2 Mpc; the distribution of the combined sample falls off strongly at a linear size of 2 Mpc. This sharp decrease was not clear from the sample of 'old' GRGs only, due to the small number of sources. In Sect. 5.4 we will discuss whether the observed cut-off is a result of selection effects or an intrinsic property of the population of GRGs.

4.2.4. Radio power distribution

We calculated the emitted radio power at a rest-frame frequency of 325 MHz assuming isotropic emission. Since the redshifts are low, the radio K-correction is only small. For the new GRGs the measured spectral index between 325 and 1400 MHz has been used; for the 'old' GRGs a spectral index of -0.8 has been assumed if no reliable literature value could be found. The distribution of 325-MHz radio powers has been plotted in Fig. 1d. Despite the fact that a large number of GRGs has been found at flux density values well below that of the 'old' sample, the distribution of the radio powers of the new sources largely overlaps that of the old sources. This is related to the, on average, higher redshifts of the new sources. The combined sample is distributed rather uniformly between 10^{25} and 10^{27} W Hz^{-1}; the sharp peak at the radio power bin centered on $10^{26.1}$ W Hz^{-1} is most likely a result of small number statistics. At 325 MHz, the traditional separation between FRII and FRI-type sources (Fanaroff & Riley 1974) lies near 10^{26} W Hz^{-1}, which is close to the median value of the combined sample (see Tab. 2).

5. Discussion

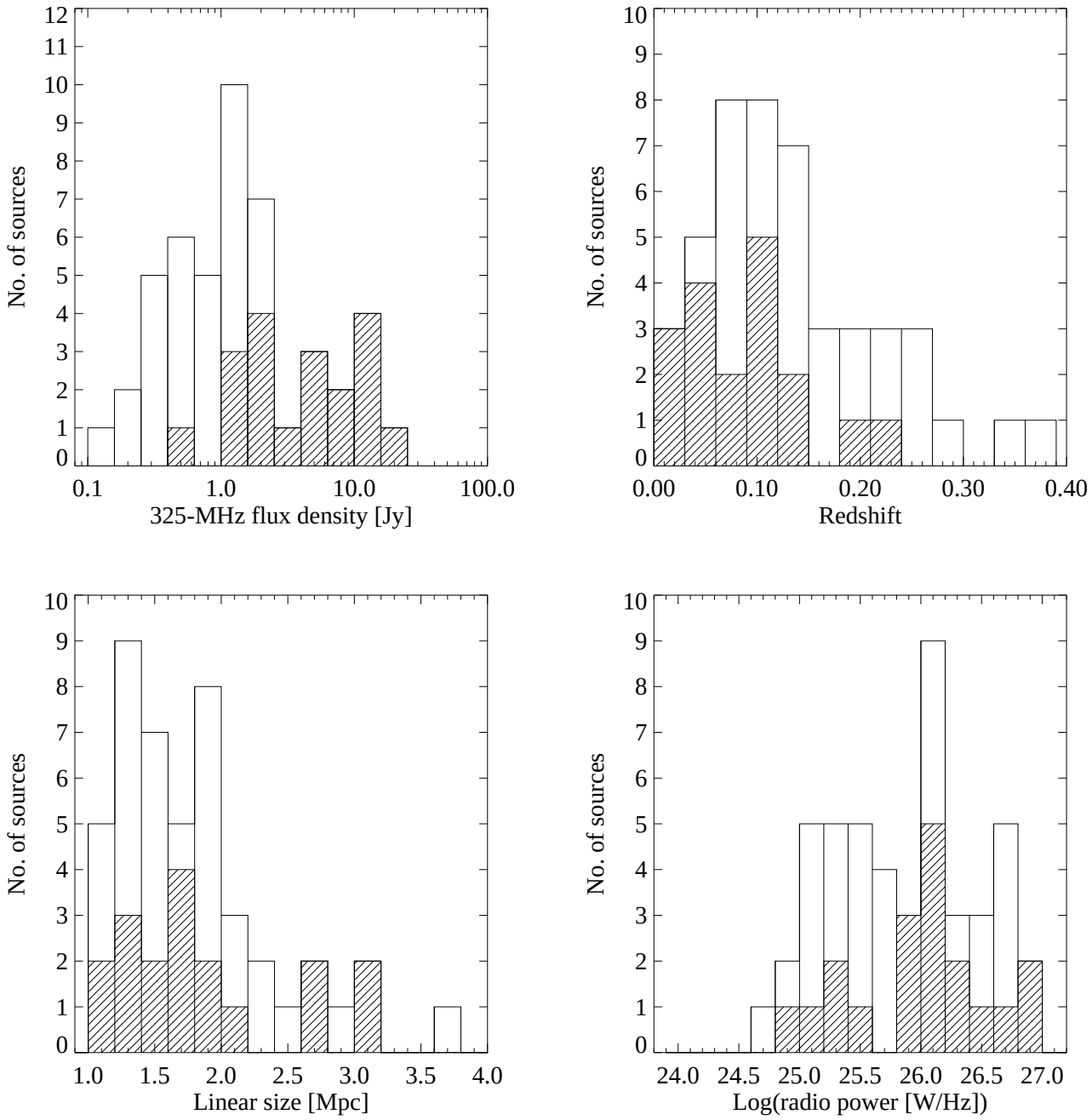

Fig. 1. Histograms of several properties of the new and old sample of GRGs. In all plots, the hatched bars indicate the distribution of previously known GRGs (see Tab. 1). **a** (upper left): The 325-MHz flux density distribution of the GRGs. We have used a binsize of 0.2 in the logarithm of the flux density in Jy. **b** (upper right): The redshift distribution of the GRGs, using a binsize of 0.03 in redshift. The source 8C 0821+695 at $z = 0.538$ lies outside the range of this plot. **c** (lower left): The projected linear size distribution of the GRGs, using a binsize of 0.2 Mpc. The source 3C 236 ($D = 5.7$ Mpc) lies outside the range of this plot. **d** (lower right): The rest-frame 325-MHz radio power distribution of the GRGs, using bins of width 0.2 in the logarithm of the radio power in $\mathrm{W\,Hz^{-1}}$.

5.1. The 'sensitivity limit' of WENSS

For a radio source to be included in our sample, it must be larger than 5′ and it must have been noticed on the radio maps as a large radio source. The latter is related to a surface brightness criterion: the average surface brightness, or integrated signal-to-noise ratio, must be high enough to be detected as a single radio source structure. The integrated

Table 2. Median values of some of the properties of the GRGs in the sample of 'old' GRGs, the sample of new GRGs and the combined sample of 47 sources. Column 1 gives the property; column 2 to 4 give the median value of these properties for the old, new and combined sample, respectively.

(1) Property	(2)	(3) Median values	(4)
	Old	New	Comb.
S_{325} [Jy]	4.160	0.685	1.150
$\log(P_{325}$ [W Hz^{-1}])	26.041	25.625	25.951
Size [Mpc]	1.65	1.63	1.64
Redshift	0.099	0.1404	0.1175

signal-to-noise ratio, $(S/N)_{int}$, for a resolved radio source is given by

$$\left(\frac{S}{N}\right)_{int} \approx \frac{S_{int}}{\sigma\sqrt{A}}, \quad (1)$$

where S_{int} is the integrated flux density of the source and the surface area A is in units of beams. The surface area can be rewritten as $A = c \cdot \theta^2_{max}$, where θ_{max} is the angular size (major axis) of the radio source and c is a number that relates the angular size to the surface area (cf. the length-to-width ratio). For instance, for an elliptically shaped radio source with a length-to-width ratio of 3, $c = \frac{\pi}{(12\ln 2)} \cdot \theta^2_{beam}$ with θ_{beam} the (FWHM) beam-size of the observation. If we substitute the above expression for A in Eq. 1 we find

$$\left(\frac{S}{N}\right)_{int} \propto \frac{S_{int}}{\theta_{max}} \ . \quad (2)$$

Fig. 2 shows S_{int}/θ_{max} against θ_{max} for the sources in our sample which we have identified as GRGs. We find that the lowest values of S_{int}/θ_{max} for selected sources lie in the range between $0.02-0.03$ Jy/arcmin; the source which lies well below this line is B 1044+745, which is one of the two sources that were selected only for its radio structure in the NVSS and should therefore be situated below the WENSS 'sensitivity' limit. The other source which lies just below the line is B 1245+676, which was selected from the WENSS but can be considered a 'border-line' case. The two sources just above the limit are B 0935+743 and B 1306+621.

The sensitivity limit appears to be almost independent of angular size at least up to a size of ~ 40 arcminute. The sensitivity of WENSS to objects with an angular size above 1 degree on the sky decreases, so that the sensitivity limit inevitably must rise eventually.

From the figure we conclude that sources with $\theta_{max} \geq 5'$ will most likely be selected if $S_{int}/\theta_{max} \gtrsim 0.025$ Jy/arcmin. We will use this criterium to specify the regions in the radio power – linear size – redshift (P, D, z) parameter space which is accessible by our selection.

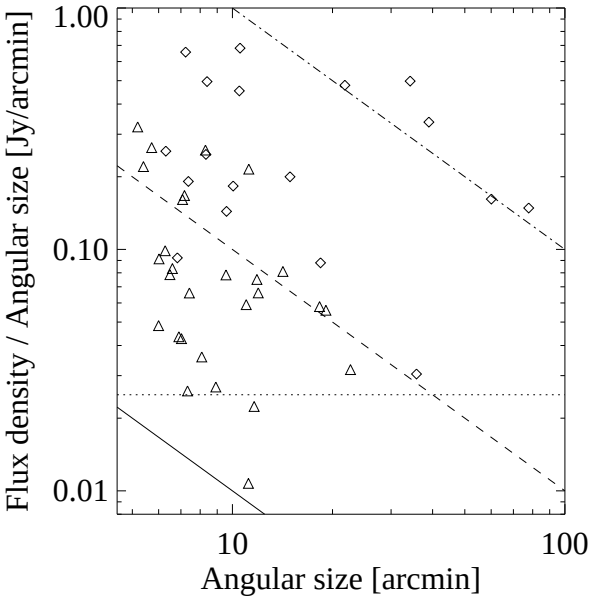

Fig. 2. A plot of the 325-MHz flux density divided by the angular size against the angular size for the 'old' (diamonds) and the newly discovered GRGs (triangles). The diagonal lines indicate a constant integrated flux density and are drawn for 0.1 (solid), 1 (dashed) and 10 (dot-dashed) Jy. From this plot we determine the sensitivity limit of our selection method, ($S_{int}/\theta_{max} = 0.025$ Jy/arcmin), indicated by the dotted horizontal line.

5.2. The radio power – linear size diagram

In Fig. 3 we have plotted for all identified GRGs in our sample the linear size, D, against the radio power at 325 MHz, P, the so-called $P-D$ diagram. For reference, all sources of the LRL sample with $z < 0.6$, which is the same redshift range as in which the GRGs are found, are plotted as well. Note that several of the formerly known GRGs are part of the LRL sample; these have been plotted as LRL sources.

From this plot the following can be concluded. First, although we have conducted the most extensive systematic search for GRGs to date, there are no sources in the upper right part of the $P-D$ diagram, i.e. the region occupied by sources with large size and high radio power. If such sources had existed in our search area, They would most likely have discovered because of their inevitable high flux density. Second, the few GRGs which have a linear size above 2 Mpc have, on average, a higher radio power than smaller-sized GRGs.

To investigate which region of the $P-D$ diagram is accessible through our WENSS selection, we have plotted in Fig. 4 lines which represent the lower sensitivity limit at constant redshift. Since the sensitivity limit is set by $S_{int}/\theta_{max} = 0.025$ Jy/arcmin (see Section 5.1), and a given redshift $S_{int} \propto P$ and $\theta_{max} \propto D$, the limit at that redshift follows the relation $P \propto D$. In Fig. 4 we have assumed a

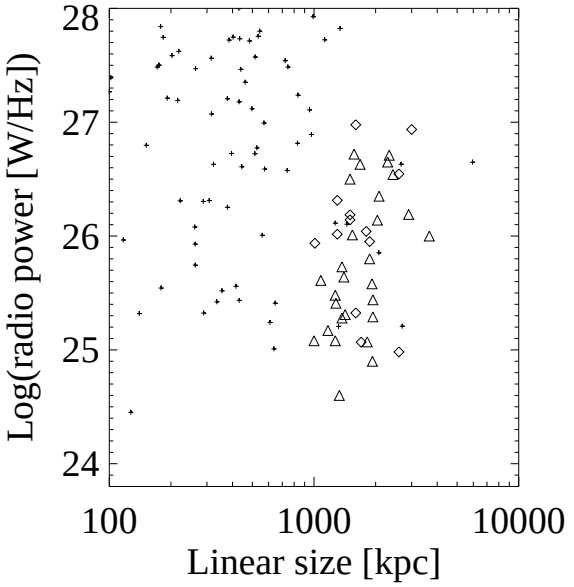

Fig. 3. The 325-MHz radio power against linear size ($P-D$ diagram) for the formerly known GRGs not part of the LRL sample (diamonds), the newly discovered GRGs (triangles) and sources from the LRL sample with $z < 0.6$ (plusses).

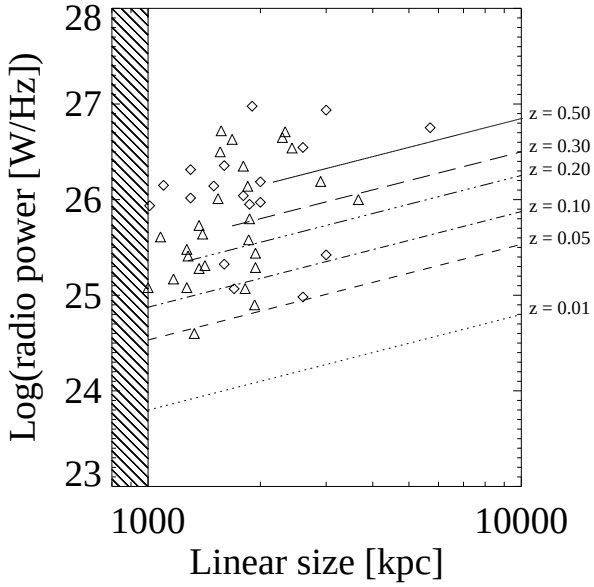

Fig. 4. $P-D$ diagram, filled with formerly known GRGs (diamonds) and newly discovered GRGs (triangles). The lines indicate the lower radio power limit for a source at a particular redshift as a function of linear size; the area directly above such a line is the accessible region in the (P, D) parameter space at that redshift. See text for further details.

radio source spectral index of -0.8 to convert flux density into radio power.

At a particular redshift, WENSS can only detect giant sources which are more powerful than the radio power at which the line has been drawn (i.e only in that part of the $P-D$ diagram which is situated above the line). Note that lines of higher redshifts also start at a larger linear size because of the $5'$ lower angular size limit we have imposed. Based on the accessible regions in the $P-D$ diagram there is no apparent reason why sources larger than 2 Mpc should be missed.

5.3. Radio power and linear size versus redshift

In Fig. 5a we have plotted the 325-MHz radio powers of the GRGs against their redshifts. The higher sensitivity of the WENSS, as compared to earlier surveys, has enabled the discovery of GRGs with $5-10$ times lower radio power. The hatched region in the figure indicates the part of the parameter space which is not accessible by WENSS, as a result of its limited sensitivity and lower angular size limit. Again, in determining this region we have assumed a spectral index of -0.8 for the radio sources, but the upper edge of the region is not very sensitive to the spectral index.

The broken shape of the upper edge of the hatched region can be understood as follows. At all redshifts, the WENSS is most sensitive to physically, and thus spatially, small sources. Since both a lower angular and physical size limit have been imposed, there are two regimes in which each of these two limits is in effect. At very low redshifts, a source with a physical size of 1 Mpc extends over $5'$ on the sky. This leads to a surface brightness limit and the integrated flux density of the source thus has to be large for the source to be still detectable. At higher redshift, the selection is constrained by the $5'$ lower angular size limit. This results in a lower limit to the flux density of a detectable source, determined by $S_{int} \geq 0.025$ [Jy/arcmin] $\cdot$ 5 [arcmin] $= 0.125$ Jy. Thus, we are flux density limited. The break occurs at that redshift at which a 1-Mpc large radio source will span an angle of $5'$ on the sky ($z \sim 0.146$).

The one source that just lies in the hatched area where no sources should have been found is B 1044+745, which, as mentioned before, would indeed not have been selected on basis of the WENSS data.

The strong effect that the lower angular size limit has on the selection can best be seen in Fig. 5b, where we have plotted the projected linear size of the identified GRGs against their redshift. Again, the hatched area indicates the region of the diagram which is inaccessible. The strong 'bump' at redshifts above ~ 0.15 result from the lower angular size limit.

Furthermore, in Fig. 5b we have plotted the sensitivity limit for sources of constant radio power (dashed lines). The (logarithm of the) radio power (in W Hz^{-1} at 325 MHz) for each particular line has been indicated at the

top of the diagram. A radio source of radio power P and linear size D can only be selected if it has redshift below that indicated by the dashed line for power P at size D. Had that source been at a higher redshift, or had it been of larger linear size, it would not have been selected. Likewise, all sources which lie on the left of such a line of constant P, should all have a radio power below this value. Apart from the before-mentioned case of B 1044+745, this is indeed the case for the identified GRGs in our sample.

5.4. The 2-Mpc linear size cut-off

A strong drop in the number of sources with projected linear size above 2 Mpc has been found (see Fig. 1c). This may be a result of a strong negative radio power evolution of radio sources with increasing size, combined with our sensitivity limit. A negative radio power evolution is indeed expected for active radio radio sources (cf. Kaiser et al. 1997, Blundell et al. 1999). On the other hand, the observed effect can also be caused if a substantial fraction of the GRGs stop their radio activity (and 'fade') before they reach a size of 3 Mpc.

Above, we have argued that the selection effects alone provide no apparent reason why sources of linear size above 2 Mpc should have been missed if they existed in large numbers. On the contrary, Fig. 5b) shows that sources above 2 Mpc in size can potentially be selected out to much higher redshift than smaller sized sources. Indeed, the figure shows that the majority of identified $2-3$ Mpc large sources have redshifts at which 1-Mpc large sources would not have been selected.

Therefore, the observed 2-Mpc cut-off must be caused by a combination of the internal luminosity evolution of the sources and the sensitivity of the WENSS. An extreme case of such a luminosity evolution occurs when a large fraction of giant sources do not remain active for a long enough amount of time to reach a linear size of 2 Mpc. To disentangle the effects of the luminosity evolution of active and so-called 'relic' sources on the observed number of sources as a function of linear size requires much better statistics on the death-rate of radio galaxies as a function of radio power and linear size.

Acknowledgments

The INT and WHT are operated on the island of La Palma by the Isaac Newton Group in the Spanish Observatorio del Roque de los Muchachos of the Instituto de Astrofisica de Canarias. The Westerbork Synthesis Radio Telescope (WSRT) is operated by the Netherlands Foundation for Research in Astronomy (NFRA) with financial support of the Netherlands Organization for Scientific Research (NWO). The National Radio Astronomy Observatory (NRAO) is operated by Associated Universities, Inc., and is a facility of the National Science Foundation (NSF). This research has made use of the NASA/IPAC Extragalactic Database (NED) which is operated by the Jet Propulsion Laboratory, California Institute of Technology, under contract with the National Aeronautics and Space Administration. The Digitized Sky Surveys were produced at the Space Telescope Science Institute under U.S. Government grant NAG W-2166. The images of these surveys are based on photographic data obtained using the Oschin Schmidt Telescope on Palomar Mountain and the UK Schmidt Telescope. The plates were processed into the present compressed digital form with the permission of these institutions. M.N. Bremer, H. Sangheera and D. Dallacasa are thanked for their help in the early stages of this project. P. Best and M. Lehnert are thanked for many helpful discussions and suggestions. L. Lara is acknowledged fro providing high resolution radio maps of several sources prior to publication.

References

Barthel, P.D. 1989, ApJ, 336, 606
Becker, R., White, R., Helfand, D. 1995, ApJ, 450, 559
Bhatnagar, S., Gopal-Krishna, Wisotzki, L. 1998, MNRAS, 299, L25
Blundell, K., Rawlings, S., Willott, C.J. 1999, AJ, 117, 677
Burbidge, E.M., Strittmattar, P.A. 1972, ApJ, 172, L37
van Breugel, W.J.M., Willis, A.G. 1981, A&A, 96, 332
van Breugel, W.J.M., Jägers W. 1982, A&AS, 49, 529
de Bruyn, A.G. 1989, A&A, 226, L13
Colla, G., Fanti, C., Fanti, R., et al. 1975, A&AS, 20, 1
Condon, J.J., Cotton, W.D., Greisen, E.W., et al. 1998, AJ, 115, 1693
Demoulin, M. 1970, ApJ, 160, L79
Dingley, S.J. 1990, Ph.D.-Thesis, University of Cambridge
Djorgovski, S.G., Thompson, D., Vigotti, M., Grueff, G. 1990, PASP, 102, 113
Djorgovski, S.G., Thompson, D., Maxfield, L., Vigotti, M., Grueff, G. 1995, ApJS, 101, 255
Falle, S.A.E.G. 1991, MNRAS, 250, 581
Fanaroff, B.L., Riley, J.M. 1974, MNRAS, 167, 31
Faulkner, M.A 1985, Ph.D.-Thesis, Univ. of Cambridge
Fomalont, E.B., Bridle, A.H. 1978, AJ, 83, 7
de Grijp, M.H.K., Keel, W.C., Miley, G.K., Goudfrooij, P., Lub, J. 1992, A&AS, 96, 389
Hine, R.G., 1979, MNRAS, 189, 527
Ishwara-Chandra, C.H., Saikia, D.J. 1999, MNRAS, 309, 100
Jägers, W.J. 1986, Ph.D.-thesis, University of Leiden
Kaiser, C.R., Alexander, P. 1999, MNRAS, 302, 515
Kaiser, C.R., Dennett-Thorpe, J., Alexander, P. 1997, MNRAS, 292, 723
Lacy, M., Rawlings, S., Saunders, R., Warner, P.J. 1993, MNRAS, 264, 721
Laing, R.A., Riley, J.M., Longair, M.S. 1983, MNRAS, 204, 151
Lara, L., Cotton, W.D., Feretti, L., et al. 2001, A&A, *in press*
Mack, K.-H., Klein, U., O'Dea, C.P., Willis, A.G. 1997, A&AS, 123, 423
Mack, K.-H., Klein, U., O'Dea, C.P., Willis, A.G., Saripalli, L. 1998, A&A, 329, 431
Marcha, M.J.M., Browne, I.W.A., Impey, C.D., Smith, P.S. 1996, MNRAS, 281, 425
Masson, C.R. 1979, MNRAS, 187, 253
Miley, G.K., Osterbrock, D.E. 1979, PASP, 92, 257
Palma, C., Bauer, F.E., Cotton, et al. 2000, AJ, 119, 2068

Parma, P., de Ruiter, H.R., Mack, K.-H., et al. 1996, A&A 306, 708
Parma, P., Murgia, M., Morganti, R., et al. 1999, A&A, 344, 7
Perley, R.A., Bridle, A.H., Willis, A.G. 1984, ApJS, 54, 291
Rengelink, R., Tang, Y., de Bruyn, A.G., et al. 1997, A&AS, 124,259
Riley, J.M. 1989, MNRAS, 238, 1055
Riley, J.M., Warner, P.J., Rawlings, S., et al. 1988, MNRAS, 236, 13
Röttgering, H.J.A., Tang, Y., Bremer, M.A.R., et al. 1996, MNRAS, 282, 1033
Sargent, W.L.W. 1973, ApJ, 182, L13
Saunders, R.D.E. 1982, Ph.D.-Thesis, University of Cambridge
Saunders, R.D.E., Baldwin, J.E., Warner, P.J. 1987, MNRAS, 225, 713
Saripalli, L., Gopal-Krishna, Reich, W., Kühr, H. 1986, A&A, 170, 20
Scheuer, P.A.G. 1974, MNRAS, 166, 513
Schoenmakers, A.P. 1999, Ph.D.-Thesis, Utrecht University
Schoenmakers, A.P., de Bruyn, A.G., Röttgering, H.J.A., van der Laan, H. 1999, A&A, 341, 44
Schoenmakers, A.P., de Bruyn, A.G., Röttgering, H.J.A., van der Laan, H., Kaiser, C.R. 2000a, MNRAS, 315, 371
Schoenmakers, A.P., Mack, K.-H., de Bruyn, A.G., et al. 2000b, A&AS, 146, 293
Simien, F., Prugniel, P. 1997, A&AS, 122, 521
Spinrad, H., Djorgovski, S., Marr, J., Aguilar, L. 1985, PASP, 97, 932
Strom, R.G., Willis, A.G. 1980, A&A, 85, 36
Strom, R.G., Baker J.R., Willis, A.G. 1981, A&A, 100, 220
Strom, R.G., Fanti, R., Parma, P., Ekers, R.D. 1983, A&A, 122, 305
Subrahmanyan, R., Saripalli, L. 1993, MNRAS, 260, 908
Vigotti, M., Grueff, G., Perley, R., Clark, B.G., Bridle, A.H. 1989, AJ, 98, 419
Wagett, P.C., Warner, P.J., Baldwin, J.E. 1977, MNRAS, 181, 465
Wieringa, M., 1991, Ph.D.-Thesis, University of Leiden
Willis, A.G., Strom, R.G., Wilson, A.S. 1974, Nat., 260, 625
Willis, A.G., Strom, R.G., Bridle, A.H., Fomalont, E.B. 1981, A&A, 95, 250

Appendix A: The sample of newly discovered GRGs and their properties

Here, we present notes on the radio structure, the host galaxies and the optical spectra of the sources. Tab. A.3 presents the flux densities and positions of the radio cores and the host galaxies. Tab. A.4 lists several other radio properties and the redshifts of the sources. Further, we present a table with the log of the INT observations (Tab. A.2) and a table with the wavelengths and redshifts of spectral emission and absorption features we have measured in the spectra of the sources (Tab. A.5). Finally, we present the radio and optical images of the sources, and the optical spectra of their host galaxies. Radio contour plots mostly are from the WENSS and/or the NVSS surveys. The FWHM beam size is indicated in a separate panel, usually situated in the lower left corner of the contour plot. The flux density level of the first contour can be found in Tab. A.6. Unless indicated otherwise in this table, contour levels have been plotted at $(-1, 1, 2, 4, 8, 16, 32, 64, 128, 256)$ times the flux density level of the first contour. For the 1.4-GHz WSRT observations, Tab. A.6 also gives the major and minor axes (FWHM) of the restoring beam. Also, we present overlays of our highest resolution radio map with the optical fields, usually retrieved from the digitized POSS-I survey, or POSS-II whenever available (see Tab. A.6). The range of grey scales is such that the contents of the optical field is shown best. In case the identification of the host galaxy of the radio source is not apparent from the optical image, we have encircled it or used an arrow to point it out. The optical spectra of the host galaxies have the identified emission and absorption features indicated. In the plots of the spectra, the '$\oplus$'-symbol indicates the presence of an atmospheric feature, such as an imperfectly subtracted bright sky-line or an atmospheric absorption band. The '$\downarrow$'-symbol indicates the presence of a feature resulting from a cosmic ray impact that could not be properly removed from the data.

B 0211+326: This $\sim 5'$-large radio source has been shortly observed with the WSRT, but no radio core has been detected. On the POSS-II image we find a small group of faint galaxies situated halfway between the two radio lobes. The brightest of these is most likely the host galaxy, since its optical spectrum shows bright emission lines. We find a redshift of 0.2605, so that the projected linear size of the radio source is 1.6 Mpc.

B 0217+367: An overlay of a 1.4-GHz WSRT radio map with the optical field shows that a ~ 10 mag. galaxy coincides with a central compact radio structure. A higher resolution 2.7-GHz map presented by Faulkner (1985) shows a radio core with two jets. The western jet is bend and has a bright knot at a distance of $20''$ from the core. Only the western radio lobe is connected to this radio core by a faint bridge. The lobe itself shows several twists and a diffuse outer structure which is only barely detected in the NVSS. The optical spectrum of the host galaxy shows weak [NII]6584 and [SII]6717/6731 emission lines. The redshift of the host galaxy is 0.0368, yielding a projected linear size of 0.95 Mpc.

B 0648+733: The compact radio source located between the two radio lobes coincides with a galaxy on the POSS-I plates. A more sensitive VLA observation shows that the western lobe has an edge-brightened radio structure (Lara et al. 2001); our WSRT map only shows the bright hotspot. The optical spectrum of the identification shows strong emission lines. The redshift is 0.1145, yielding a projected linear size of 2.0 Mpc. The compact source overlapping with the eastern radio lobe on the NVSS radio map is most likely an unrelated background source.

B 0648+431: This $\sim 10'$-large radio source consists of four main components. An overlay of the 1.4-GHz WSRT radio map with an optical image shows that the eastern of the two middle component coincides with a 12 mag. optical galaxy. An optical spectrum of the galaxy shows weak [NII]6548,6583 line-emission on top of a stellar continuum, at a redshift of 0.0891. The projected linear size of the radio source is 1.3 Mpc.

B 0658+490: In the WENSS radio map this source is an $\sim 19'$-large complicated radio structure with a fairly diffuse eastern part, three compact sources in the middle and a diffuse western extension. The FIRST survey has resolved the central source, and shows that it has a jet-like extension in the direction of a larger jet-like feature on the NVSS radio map. The central source coincides with an 11 mag. Optical galaxy, whose optical spectrum shows weak [NII]6548/6583 emission. The redshift is 0.0650. The two bright compact sources west of the radio core are resolved in the FIRST survey. The westernmost one appears to be an edge-brightened radio lobe, the other is more compact and has a radio tail pointing away from the radio core. It is unclear if this component is truly associated with the large radio source. If it were an unrelated source, the lack of an optical identification on the POSS-II survey suggests that it is at a much higher redshift than the host galaxy of the central radio source. Assuming that all radio structures are part of a single radio source, it has a linear size of 1.9 Mpc.

B 0747+426: This is a $6'$-large radio source with a bent radio structure. The southern lobe is larger and more diffuse. Neither of the two lobes contains a bright hotspot. Near the central bent a 17 mag. galaxy is detected which coincides with a weak, unresolved source in the FIRST survey, presumably the radio core. Its optical spectrum reveals [OII]3727 emission and a stellar continuum. The redshift is 0.2030, yielding a projected linear size of 1.5 Mpc.

B 0750+434: Although only a weak radio source in the WENSS, this object is one of the largest radio sources we have discovered in this project. The central source, unresolved by FIRST, coincides with a 16.7 mag. star-like object. An optical spectrum reveals strong emission lines, among which broad Hydrogen Balmer lines, and a blue-colored continuum. The redshift is 0.3474, which is the highest of all sources presented here. The southern radio lobe is resolved by FIRST into three separate components, of which probably only the most southern one is related to the large scale radio structure. The projected linear size of this source is 2.9 Mpc.

B 0757+477: The NVSS reveals a strong radio core in this source. The FIRST survey radio map shows that the northern lobe has a compact hotspot and that the southern lobe is diffuse. The core is unresolved by FIRST and coincides with a 15.5 mag. star-like object. The optical spectrum is dominated by strong and broad Hydrogen Balmer lines and a blue non-thermal continuum. The redshift is 0.1567, resulting in a projected linear size of the radio source of 1.3 Mpc.

B 0801+741: The 1.4-GHz WSRT observations of this source reveal a compact core, coinciding with a 15.8 mag. optical galaxy. The radio lobes are largely resolved out, however. The NVSS map suggests that these lobes are narrow and straight. The redshift of the host galaxy is 0.1204, and its sepctrum reveals Hα, [NII]6548/6583 and [SII]6717/6738 emission lines. The Hβ emission line is weak, relative to Hα, suggesting a large amount of extinction towards the line-emitting gas. The projected linear size of the radio source is 1.1 Mpc.

B 0809+454: In the WENSS and NVSS this source is a rather weak $\sim 7'$-large radio source. The FIRST survey radio map shows the radio core and the two outer extremities of the radio lobes which contain hotspots. The radio core coincides with a 18.5 mag. optical source, whose spectrum shows strong [OIII]4959,5007 and [OII]3727 emission lines. The redshift is 0.2204, yielding a projected linear size of 1.9 Mpc.

B 0813+758: This source has originally been selected from the NVSS, in which it is an $8.5'$-large radio source with a bright unresolved central source and an asymmetrical radio structure. A short 1.4-GHz WSRT observation shows that the the eastern radio lobe has a rather strange structure. Higher quality VLA data confirm that all structures on the WSRT map are part of a single large radio lobe (Lara et al. 2001). The central radio source coincides with a 17.5 mag. galaxy whose optical spectrum shows strong emission lines. The Hα-line has a broad component. We measure a redshift of 0.2324, resulting in a linear size of the radio source of 2.3 Mpc.

B 0905+352: This $6.3'$-large radio source shows no significant structure in WENSS or NVSS. FIRST, however, reveals that the two radio lobes have strong hotspots, and that the western lobe has an extension towards the north-west. No radio core is detected. Two bright compact objects halfway the two radio lobes were identified as stars, and only the galaxy surrounded by the dashed circle in Fig. A.12 was found to show a galaxy-like spectrum, although we have not yet firmly established its redshift. The two lines indicated as [NII] in the spectrum coincide with atmospheric OH-bands. If they are real, the redshift is 0.106, which is rather low considering that the galaxy has a POSS-E magnitude of 18.0 . A redshift of 0.260 can also be argued, because of a possible

4000Å-break observed at a wavelength of 5050Å. This higher redshift would agree more closely with the optical magnitude of the galaxy.

B 0925+420: This source is one of the so-called 'Double-double' radio galaxies (see Schoenmakers et al. 2000a), consisting of two separate double-lobed radio structures. Radio maps, optical images and further information are presented in Schoenmakers et al. (2000a).

B 0935+743: This source has a radio morphology much resembling that of the known giant radio galaxy 4CT 74.17 (e.g. van Breugel & Willis 1981). The central source coincides with an optical galaxy of 14.3 mag. The optical spectrum shows no signs of emission lines. A somewhat higher resolution observation shows that the central source has two jet-like features pointing towards the outer two sources (Lara et al. 2001), which suggests that all three are part of a single radio structure. The redshift of the optical galaxy associated with the radio core is 0.1215, yielding a projected linear size of 1.3 Mpc.

B 1029+281: Because of the low declination of this source, the WENSS radio map does not show much structure. The NVSS map shows a large double-lobed radio source with a relatively strong radio core. The central source is resolved by FIRST into a compact source coinciding with a 14.3 mag. optical galaxy, and a radio lobe-like feature at a distance of $\sim 1'$ to the north. This much resembles the structure observed in the so-called 'double-double' radio galaxies (Schoenmakers et al. 2000a). The optical spectrum of the host galaxy shows strong and broad Hα emission. The Hβ emission line also has a broad component. Also, it is much weaker than Hα which may indicate a high amount of internal extinction. The redshift is 0.0854, yielding a projected linear size of 1.4 Mpc.

B 1044+745: Although this radio source is clearly detected in the NVSS, it is not in the WENSS. The NVSS radio map shows two diffuse lobe-like structures with a weak, compact source in between. The compact source coincides with a 14 mag. galaxy. The optical spectrum of this galaxy is dominated by stellar continuum, with only a weak [NII]6584 emission-line. The redshift is 0.1210, and the projected linear size of the radio source is thus 1.9 Mpc.

B 1110+405: A FIRST radio map of this $12'$-large radio source shows a relatively bright component in the western radio lobe which resembles a small edge-brightened radio lobe. However, there also is diffuse radio emission at much a larger distance from the radio core. The radio core is identified with a 11.4 mag. galaxy, which appears to be double. However, the western optical object is spectroscopically identified as a star. The optical spectrum of the galaxy shows stellar continuum and weak [NII]6584 and [SII]6717/6731 emission lines although the latter lie in an atmospheric absorption band. The projected linear size of the radio source is 1.4 Mpc.

B 1144+352: This source is extensively discussed elsewhere (Schoenmakers et al. 1999b).

B 1213+422: The radio map from the FIRST survey shows two extended radio lobes and an unresolved central radio source, which coincides with a 15.9 mag. galaxy. Its optical spectrum shows strong [OIII]4959,5007 emission lines and stellar continuum. The Hα-line is clearly broadened. The redshift is 0.2426 and the projected linear size is 1.5 Mpc.

B 1245+676: This $\sim 12'$-large radio source has an inverted spectrum radio core, which is identified with a 14 mag. galaxy. An optical spectrum of this source can be found in Marcha et al. (1996); it shows no sign of emission lines. The redshift is 0.1073, and the projected linear size of the radio source is therefore 1.8 Mpc. A more detailed analysis of the radio structure of this source will be presented in de Bruyn et al. (in preparation).

B 1306+621: This $\sim 9'$-large radio source is rather faint. The WENSS and NVSS radio maps show two radio lobes and a radio core. A 1.4-GHz WSRT observation shows that both lobes are edge-brightened. The radio core coincides with a 16 mag. galaxy, which does not show any emission-lines, though. The redshift is 0.1625, yielding a projected linear size of 1.9 Mpc.

B 1310+451: On an angular scale, this is the largest radio source we have found. It has a size of $\sim 23'$ and contains a bright central core and two diffuse outer lobes. The bright compact source just beyond the western lobe is most likely an unrelated radio source. In the FIRST survey, the radio core is resolved and two jets are visible. The radio core coincides with a 10 mag. galaxy. The optical spectrum shows that it has weak [NII]6584 and [SII]6717/6731 emission lines. It has a redshift of 0.0358, yielding a projected linear size of 1.4 Mpc. The existence of the large scale radio emission and the redshift of this radio source have been reported earlier by Faulkner (1985).

B 1416+380: This $\sim 7'$-large radio source resembles a fat double radio source. The northern radio lobe is barely detected in the NVSS. The integrated spectral index of the whole source between 325 and 1400 MHz is -1.46, which makes this radio source the steepest spectrum radio source in our sample. The central component is unresolved in the FIRST and it coincides with a 14.5 mag. galaxy. The optical spectrum of this galaxy shows [OI]6300, Hα and [NII]6548/6584 emission. Its

redshift is 0.1350, resulting in a projected linear size of 1.4 Mpc.

B 1426+295: The eastern lobe of this $\sim 15'$-large source is situated near a bright, but unrelated radio source. The FIRST radio map shows an unresolved central object, which coincides with a 13 mag. optical galaxy. The optical spectrum of this galaxy shows weak emission lines of [NII]6548/6583, Hα, which is partly in absorption, and [SII]6717/6731. The redshift is 0.087, resulting in a projected linear size of the radio source of 1.9 Mpc. We remark that spectroscopical observations of the galaxy situated $\sim 30''$ to the north-west of the host galaxy show that it has the same redshift and is therefore most likely part of the same group of galaxies as the host galaxy.

B 1450+333: This source is also a 'Double-double' radio galaxy. Radio maps, optical images and further information are presented in Schoenmakers et al. (2000a).

B 1543+845: This source has been found in the NVSS maps, before the WENSS maps of this region of the sky became available. It shows an $8'$-large double-lobed radio source with a weak central compact source which coincides with an optical galaxy. The identification of the compact radio source as the radio core is confirmed by a higher resolution VLA radio map (Lara et al. 2001). In the optical spectrum, which has been obtained by I.M. Gioia with the 2.2m telescope of the University of Hawaii on Mauna Kea, we have identified the [OIII] 4959/5007 emission lines. We measure a redshift of 0.201, which yields a projected linear size of 2.1 Mpc for the radio source.

B 1709+464: This $10'$-large radio source has a diffuse western lobe and a more edge-brightened eastern lobe. The radio core is clearly detected and a map from the FIRST survey shows that this source has a small two-sided structure somewhat resembling the larger scale radio structure. The core coincides with a 10 mag. optical galaxy. The spectrum reveals weak [NII]6584 and [SII]6717/6731 emission lines. The redshift of the host galaxy is 0.0368, yielding a projected linear size of 0.59 Mpc. This is therefore not a GRG.

B 1736+375: This is a $7'$-large elongated radio structure which in the NVSS map has a dominant central source. It coincides with a 15.9 mag. galaxy, whose optical spectrum reveals Hα and [NII] emission-lines, although these are situated near a strong atmospheric absorption band. The redshift is 0.1562. The northern radio structure appears to be a small double-lobed source in the NVSS, and at its center a faint optical galaxy is situated. We have no spectrum of this source. The northern structure may be an unrelated radio source. If the whole structure were to be a single radio source, the projected linear size would be 1.4 Mpc.

B 1852+507: The NVSS map of this $7'$-large radio source shows two lobes and a central component which coincides with a 12.8 mag. galaxy. We have identified the bright nearby optical source as a star. The optical spectrum of the galaxy shows no emission lines. Its redshift is 0.0958, yielding a linear size of the radio source of 1.0 Mpc.

B 1911+470: This $\sim 6'$-large radio source has a dominant central component and a somewhat bent southern radio lobe. The central component coincides with a 12 mag. optical galaxy, which has a companion at a distance of $\sim 30''$ to the north-west. The optical spectrum shows a weak [NII]6584 emission-line, but it overlaps with an atmospheric absorption band. Its redshift is 0.0548. The companion has the same redshift and they are therefore most likely also physically close to each other. The projected linear size of the radio source is 0.54 Mpc, and therefore this is not a GRG.

B 1918+512: This $7.3'$-large radio source has a FRII-type radio morphology. The eastern 'extension' is an unrelated radio source. A deep 21-cm WSRT observation shows a possibly two-sided jet in this source and a central radio source, probably the radio core. A CCD-image obtained by P. Best with the LDSS imaging spectrograph on the 4.2m WHT telescope on La Palma shows a faint galaxy close to the core; on the DSS this source is merged with a nearby star. An optical spectrum shows possible emission lines of [OII]3727 and [OIII]5007, as well as several absorption features, all in agreement with a redshift of 0.284. We note that the star-like object situated in the 'gap' between the two radio lobes is spectroscopically identified as a star. If the redshift of the host galaxy is correct, the linear size of this radio galaxy is 2.3 Mpc.

B 2147+816: This $18'$-large FRII-type radio galaxy has been briefly described before by Saunders (1982), and more recently (and more extensively) by Palma et al. (2000). Both the NVSS and WENSS radio map show the two radio lobes and the central core. The radio core coincides with a 16.5 mag. galaxy, which is a member of a small group of three galaxies. The optical spectrum of the identification shows strong emission lines. Its redshift is 0.1457, confirming the values given by Saunders (1982) and Palma et al. (2000). The projected linear size of the radio source is 3.7 Mpc.

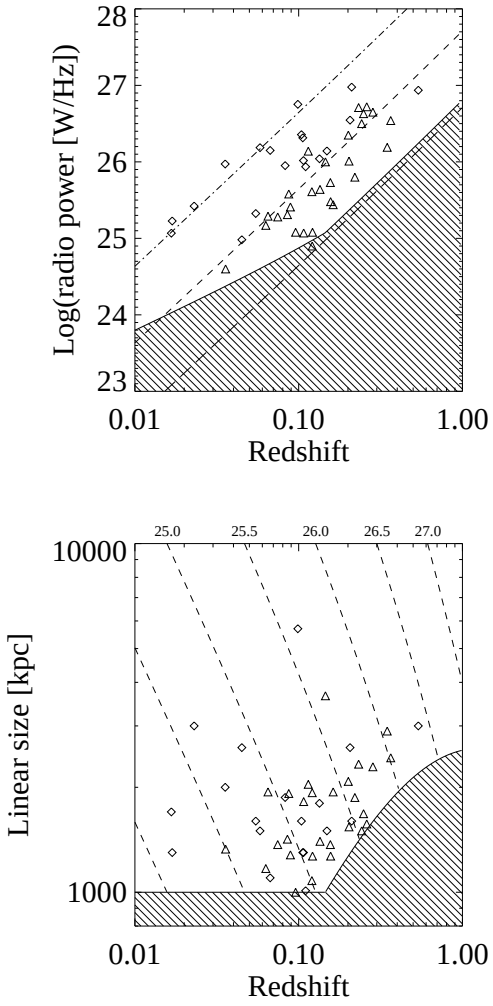

Fig. 5. **a**: (Top) The 325-MHz radio power against the redshift of the formerly known (diamonds) and newly discovered (triangles) GRGs. The three diagonal lines represent the radio power for sources with a 325-MHz flux density of 0.1 Jy (long-dashed), 1.0 Jy (dashed) and 10.0 Jy (dot-dashed), assuming a spectral index of -0.8. The hatched area indicates the part of the diagram in which sources fall below our sensitivity limit. **b**: (Bottom) The projected linear sizes of the GRGs against their redshift. The meaning of the symbols is the same as in the upper plot. The hatched area indicates the region of the plot in which sources have not been selected, either because they are physically smaller than 1 Mpc, or spatially smaller than $5'$. The dashed lines indicate the sensitivity limit for sources of the particular radio power is indicated (in logarithmic units of $\mathrm{W\,Hz^{-1}}$ at 325 MHz) on top of each line. We assume a spectral index of -0.8. Sources can only be detected if they lie to the left of the line belonging to their particular radio power.

Table A.1. Table with WENSS selected candidate GRGs after removing sources identified as non-GRGs on basis of optical data. Column 1 gives IAU-notation (in B1950.0) of the source name. Columns 2 and 3 give approximate source coordinates in Right Ascension and Declination in B1950.0 coordinates. Column 4 gives the integrated WENSS flux of the source. Column 5 gives the size of the source in arcminutes. Column 6 indicates whether the source is considered a GRG-candidate, for reasons given in column 7.

(1) Source	(2) R.A. [h m s]	(3) Dec. [$^\circ$ $'$ $''$]	(4) S_{325} [Jy]	(5) Size [$'$]	(6) Still selected?	(7) Reason/comments
B 0001+342	00 01 10	34 13 00	0.69	12	no	NVSS morphology
B 0023+750	00 23 15	75 00 30	0.30	5	yes	NVSS selected, supported by WENSS
B 0036+285	00 36 05	28 29 00	1.54	7	no	NVSS and 1.4-GHz WSRT morphology
B 0050+433	00 50 10	43 25 00	0.59	12	no	NVSS morphology
B 0058+403	00 58 05	40 19 00	1.04	5	no	NVSS morphology
B 0119+377	01 19 10	37 44 00	2.29	6	no	NVSS morphology
B 0126+426	01 26 45	42 36 00	0.79	13	no	NVSS morphology
B 0141+762	01 41 25	76 13 00	0.18	6	yes	NVSS selected, supported by WENSS
B 0200+457	02 00 10	45 45 30	0.19	6	yes	NVSS morphology
B 0200+678	02 00 30	67 53 00	2.15	6	no	1.4-GHz WSRT morphology
B 0201+317	02 01 35	31 42 00	0.15	6	no	NVSS morphology
B 0211+326	02 11 20	32 37 00	1.59	5	yes	1.4-GHz WSRT morphology
B 0217+367	02 17 20	36 46 00	2.44	16	yes	NVSS morphology
B 0330+871	03 30 35	87 07 00	0.11	6	yes	NVSS selected, supported by WENSS
B 0334+329	03 34 30	32 59 00	0.54	6	yes	NVSS morphology
B 0429+293	04 29 40	29 22 00	1.31	7	no	NVSS morphology
B 0503+704	05 03 30	70 27 00	1.01	6	no	NVSS morphology
B 0603+612	06 03 00	61 15 00	1.64	5	yes	NVSS morphology
B 0627+721	06 27 40	72 11 30	0.77	5	yes	NVSS and 1.4-GHz WSRT morphology
B 0634+515	06 34 35	51 30 00	0.36	10	yes	NVSS morphology
B 0646+370	06 46 55	37 03 00	0.47	6	no	NVSS morphology
B 0648+734	06 48 15	73 23 30	2.4	13	yes	NVSS morphology
B 0648+431	06 48 40	43 08 30	0.71	10	yes	NVSS morphology
B 0658+490	06 58 20	49 03 30	1.01	19	yes	NVSS morphology
B 0713+432	07 13 45	43 14 00	0.59	7	yes	NVSS and FIRST morphology
B 0730+375	07 30 00	37 30 00	0.52	10	no	NVSS and FIRST morphology
B 0747+426	07 47 40	42 39 00	0.64	6	yes	NVSS/FIRST morphology
B 0750+434	07 50 40	43 24 00	0.24	8	yes	NVSS/FIRST morphology
B 0757+477	07 57 55	47 44 30	0.25	6	yes	NVSS/FIRST morphology
B 0801+741	08 01 15	74 09 00	0.55	6	yes	NVSS selected, supported by WENSS
B 0809+454	08 09 40	45 25 00	0.26	7	yes	NVSS and FIRST morphology
B 0813+758	08 13 40	75 48 00	2.14	8	yes	NVSS selected, supported by WENSS
B 0817+427	08 17 45	42 43 00	1.18	9	no	NVSS and FIRST morphology
B 0817+337	08 17 50	33 43 00	0.26	6	no	NVSS and FIRST morphology
B 0840+513	08 40 45	51 18 00	0.98	10	no	NVSS and FIRST morphology
B 0853+292	08 53 00	29 16 00	3.90	15	no	NVSS and FIRST morphology
B 0854+402	08 54 00	40 12 00	0.35	6	no	NVSS and FIRST morphology
B 0903+783	09 03 11	78 21 30	0.20	8	no	Western 'lobe' overlaps bright spiral galaxy
B 0905+352	09 05 45	35 17 30	0.57	6	yes	NVSS and FIRST morphology
B 0909+353	09 09 45	35 22 00	0.50	6	yes	NVSS and FIRST morphology
B 0917+307	09 17 15	30 42 30	0.46	10	no	NVSS and FIRST morphology
B 0925+420	09 25 55	42 00 00	0.55	7	yes	NVSS and FIRST morphology
B 0935+743	09 35 00	74 19 00	0.19	7	yes	NVSS selected, supported by WENSS
B 0936+512	09 36 40	51 17 30	0.94	6	no	WSRT 1.4-GHz and FIRST morphology
B 1001+548	10 01 30	54 48 30	0.52	13	yes	NVSS morphology
B 1029+281	10 29 25	28 11 30	0.67	11	yes	NVSS and FIRST morphology
B 1029+322	10 29 40	32 12 00	0.64	11	no	WSRT 1.4-GHz and FIRST morphology
B 1030+312	10 30 25	31 12 00	0.87	6	no	NVSS and FIRST morphology
B 1036+632	10 36 30	63 15 30	0.14	5	yes	NVSS morphology
B 1044+745	10 44 15	74 35 30	0.12	11	yes	NVSS selected, supported by WENSS
B 1054+488	10 54 10	48 52 30	0.71	8	yes	NVSS and FIRST morphology

Continued on next page...

...Continued from previous page

(1) Source	(2) R.A. [h m s]	(3) Dec. [$^\circ$ $'$ $''$]	(4) S_{325} [Jy]	(5) Size [$'$]	(6) Still selected?	(7) Reason/comments
B 1110+405	11 10 20	40 34 00	0.82	12	yes	NVSS and FIRST morphology
B 1112+333	11 12 15	33 19 00	3.06	6	no	WSRT 1.4-GHz and FIRST morphology
B 1144+353	11 44 45	35 18 30	0.97	12	yes	$z = 0.063$ (NED), so $D \sim 1.2$ Mpc
B 1150+312	11 50 50	31 12 00	0.28	9	no	NVSS and FIRST morphology
B 1209+614	12 09 30	61 04 00	2.54	6	no	4C 61.25, NVSS morphology
B 1213+422	12 13 40	42 16 00	1.10	5	yes	NVSS and FIRST morphology
B 1218+639	12 18 30	63 56 30	1.19	8	no	NVSS morphology
B 1232+535	12 32 40	53 35 00	0.36	10	yes	NVSS morphology
B 1234+836	12 34 00	83 39 30	0.07	6	yes	NVSS selected, supported by WENSS
B 1245+676	12 45 30	67 39 00	0.20	12	yes	NVSS selected, $z = 0.1073$ (NED), so $D \sim 1.8$ Mpc
B 1250+452	12 50 45	45 17 00	1.33	10	no	NVSS morphology and bright optical ID
B 1306+621	13 06 50	62 10 00	0.19	9	yes	NVSS morphology
B 1310+451	13 10 05	45 09 30	0.65	23	yes	$z = 0.0356$ (NED), so $D \sim 1.4$ Mpc
B 1330+361	13 30 20	36 09 00	0.27	7	no	NVSS and FIRST morphology
B 1340+382	13 40 50	38 15 00	0.34	10	yes	NVSS and FIRST morphology
B 1340+447	13 40 55	44 44 00	0.30	6	no	NVSS and FIRST morphology
B 1342+407	13 42 30	40 44 00	0.51	8	no	NVSS and FIRST morphology
B 1343+371	13 43 45	37 07 00	1.90	7	no	WSRT 1.4-GHz and FIRST morphology
B 1404+362	14 04 55	36 15 00	0.24	6	no	NVSS and FIRST morphology
B 1415+685	14 15 30	68 33 00	0.26	6	yes	NVSS morphology
B 1416+380	14 16 35	38 00 00	0.46	7	yes	NVSS and FIRST morphology
B 1426+295	14 26 10	29 32 00	1.10	15	yes	NVSS and FIRST morphology
B 1443+310	14 43 20	31 04 00	0.41	7	yes	NVSS and FIRST morphology
B 1450+333	14 50 55	33 21 00	1.38	6	yes	NVSS and FIRST morphology
B 1532+315	15 32 40	31 35 00	0.73	13	no	NVSS and FIRST morphology
B 1535+613	15 35 40	61 22 00	0.09	6	no	NVSS morphology
B 1543+845	15 43 55	84 33 00	1.14	8	yes	NVSS selected, supported by WENSS
B 1614+485	16 14 25	48 33 00	0.17	10	yes	NVSS and FIRST morphology
B 1623+410	16 23 30	41 03 00	1.25	7	no	NVSS and FIRST morphology
B 1634+503	16 34 15	50 23 00	0.59	7	no	NVSS and FIRST morphology
B 1637+539	16 37 50	53 55 00	1.99	9	no	NVSS and FIRST morphology
B 1639+328	16 39 05	32 50 00	0.90	6	no	NVSS and FIRST morphology
B 1709+464	17 09 30	46 28 00	1.11	10	yes	NVSS and FIRST morphology
B 1736+375	17 36 40	37 35 00	0.48	7	yes	NVSS morphology
B 1838+658	18 38 05	65 52 00	0.95	7	yes	NVSS; $z = 0.23$ (NED), so $D \sim 1.9$ Mpc.
B 1844+653	18 44 00	65 19 10	0.26	7	yes	NVSS morphology
B 1852+507	18 52 20	50 42 00	0.27	7	yes	NVSS morphology
B 1855+310	18 55 20	31 00 00	1.35	9	yes	NVSS morphology
B 1911+470	19 11 50	47 01 00	0.80	6	yes	NVSS morphology
B 1911+481	19 11 50	48 09 00	0.77	16	yes	NVSS morphology
B 1918+453	19 18 40	45 22 00	0.78	18	yes	NVSS morphology
B 1918+516	19 18 05	51 36 00	1.22	7	yes	NVSS morphology
B 1919+479	19 19 55	47 59 30	3.52	10	yes	4C47.51, $z = 0.102$ (NED), so $D \sim 1.5$ Mpc
B 1919+741	19 19 15	74 09 30	2.04	6	yes	NVSS morphology
B 1924+549	19 24 30	54 59 00	0.48	7	no	NVSS morphology
B 2130+341	21 30 05	34 07 00	0.37	6	yes	NVSS morphology
B 2147+816	21 47 20	81 41 00	1.06	18	yes	NVSS selected, supported by WENSS
B 2205+376	22 05 25	37 36 00	0.32	7	yes	NVSS morphology
B 2231+320	22 31 10	32 00 00	0.29	11	no	NVSS morphology
B 2233+373	22 33 20	37 20 00	0.62	6	yes	NVSS morphology
B 2312+419	23 12 40	41 57 10	0.27	6	no	NVSS morphology
B 2315+401	23 15 55	40 10 17	0.11	6	yes	NVSS morphology
B 2326+315	23 26 00	31 35 00	0.47	10	no	NVSS morphology
B 2357+401	23 57 10	40 08 00	0.22	5	yes	NVSS morphology

Table A.2. Log of the spectroscopic observations of GRG candidates in our sample. Column 1 gives the name of the source in IAU format. Column 2 gives the telescope used for the observations. Column 3 gives the observing date. Column 4 gives the central wavelength of the observation in Ångstrom (for the INT only). Column 5 gives the used width of the slit in arcsec. Column 6 gives the integration time. Column 6 gives an indication of the observing conditions; 'P' stands for photometric conditions, 'NP' for non-photometric conditions, or cirrus clouds, and 'C' stands for cloudy conditions.

(1) Source	(2) Tel.	(3) Date	(4) $\lambda_{\rm central}$ [Å]	(5) Slit [″]	(6) Int. [s]	(7) Cond.
B 0211+326	INT	4 Aug. 1995	6000	2	2400	NP
		8 Oct. 1996	6500	2	1200	P
B 0217+367	INT	4 Aug. 1995	5500	2	900	C
B 0648+733	INT	6 Apr. 1996	6000	2	1800	P
B 0648+431	INT	7 Apr. 1996	6000	2	1200	NP
B 0658+490	INT	6 Apr. 1996	6000	2	1800	P
B 0747+426	INT	8 Oct. 1996	6000	2	1200	P
B 0750+434	INT	9 Oct. 1996	6000	2	600	P
			6500	2	600	P
B 0757+477	INT	7 Apr. 1996	5500	2	600	NP
			6500	2	600	NP
B 0801+741	INT	7 Apr. 1996	6000	2	600	NP
B 0809+454	INT	8 Apr. 1996	6000	3	600	NP
			6500	3	600	NP
B 0813+758	INT	6 Apr. 1996	6000	2	600	P
			6500	2	1200	P
B 0905+352	INT	7 Apr. 1996	6000	2	600	NP
B 0925+420	INT	8 Apr. 1996	6000	2	600	NP
B 0935+743	INT	7 Apr. 1996	6000	2	1200	NP
B 1029+281	INT	7 Apr. 1996	6000	2	1200	NP
B 1044+745	INT	7 Apr. 1996	6000	2	600	NP
B 1110+405	INT	6 Apr. 1996	6000	2	1200	P
B 1213+422	INT	7 Apr. 1996	6000	2	600	NP
			6500	2	600	NP
B 1306+621	INT	8 Apr. 1996	6000	2	1200	NP
B 1310+451	INT	5 Aug. 1995	5500	2	900	P
B 1416+380	INT	5 Aug. 1995	6000	2	900	P
		9 Apr. 1996	6500	2	600	P
B 1426+295	INT	4 Aug. 1995	5500	2	1800	P
		9 Apr. 1996	6000	2	1200	P
B 1450+333	WHT	8 July 1997		2	600	P
B 1543+845	2.2m UH	4 Mar. 1998		2	2100	P
		5 Mar. 1998		2	2400	P
B 1709+464	INT	4 Aug. 1995	5500	2	900	P
B 1736+375	INT	9 Oct. 1996	6000	2	1200	P
B 1852+507	INT	9 Oct. 1996	6000	2	600	P
B 1911+470	INT	8 Oct. 1996	6000	2	1200	P
B 1918+516	INT	8 Oct. 1996	6000	2	600	P
B 2147+816	INT	9 Oct. 1996	5500	2	600	P
			6000	2	1200	P

Table A.3. Properties of the radio cores and the optical identifications of the spectroscopically observed sources, and of the confirmed giant sources B 1144+352, B 1245+676 and B 1310+451. Column 1 gives the name of the radio source in IAU notation; column 2 gives the observation used to determine the radio core position and its flux density; columns 3 and 4 give the radio core position in right ascension and declination, respectively, in B1950.0 coordinates. These have been obtained by fitting a Gaussian in the radio map. Column 5 gives the integrated flux density at 1.4 GHz of the radio core. Columns 6 and 7 give the position of the optical identification in right ascension and declination, respectively, in B1950.0 coordinates, obtained from fitting a Gaussian in the available optical image. Column 8 gives the magnitude of the identification in the red (POSS-E) band of the Palomar survey. The magnitudes for sources weaker than 15.0 have been obtained from the APM catalogue and are estimated to be accurate to 0.5 mag. For brighter sources, we have measured the magnitudes directly from the digitized POSS-I frames using the photometric calibration for stars available from the STScI WWW-pages and through the GETIMAGE-2.0 plate retrieval software. Typical uncertainties in these values are estimated to be large, at least 1 mag.

(1)	(2)	(3)	(4)	(5)	(6)	(7)	(8)
		Radio			Optical		
Source	Obs.	R.A. (B1950.0)	Dec.	Flux [mJy]	R.A. (B1950.0)	Dec.	Mag.
B 0211+326	WSRT			< 2.7	02 11 18.11 ± 0.02	32 37 06.8 ± 0.2	17.6
B 0217+367	WSRT	02 17 21.78 ± 0.01	36 45 58.1 ± 0.1	64.1 ± 3.3	02 17 22.02 ± 0.02	36 45 56.7 ± 0.3	10.0
B 0648+733	WSRT	06 48 14.35 ± 0.15	73 23 33.1 ± 0.8	2.3 ± 0.2	06 48 15.01 ± 0.01	73 23 32.9 ± 0.2	15.7
B 0648+431	WSRT	06 48 43.34 ± 0.02	43 08 38.8 ± 0.3	36.2 ± 2.1	06 48 43.44 ± 0.02	43 08 36.4 ± 0.2	11.7
B 0658+490	FIRST	06 58 18.36 ± 0.01	49 03 40.9 ± 0.1	14.2 ± 0.5	06 58 18.11 ± 0.01	49 03 37.0 ± 0.1	10.9
B 0747+426	FIRST	07 47 40.54 ± 0.03	42 39 04.9 ± 0.4	1.1 ± 0.2	07 47 40.65 ± 0.01	42 39 04.0 ± 0.1	17.0
B 0750+434	FIRST	07 50 38.63 ± 0.01	43 24 02.3 ± 0.1	14.6 ± 0.4	07 50 38.75 ± 0.01	43 24 01.1 ± 0.1	16.7
B 0757+477	FIRST	07 57 54.64 ± 0.01	47 44 36.0 ± 0.1	64.1 ± 1.3	07 57 54.78 ± 0.01	47 44 34.5 ± 0.1	15.5
B 0801+741	WSRT	08 01 15.88 ± 0.03	74 09 19.1 ± 0.2	14.1 ± 0.9	08 01 16.04 ± 0.01	74 09 17.7 ± 0.1	15.8
B 0809+454	FIRST	08 09 40.30 ± 0.02	45 25 05.1 ± 0.2	1.9 ± 0.2	08 09 40.41 ± 0.01	45 25 04.1 ± 0.1	18.5
B 0813+758	WSRT	08 13 39.58 ± 0.03	75 48 02.7 ± 0.1	32.9 ± 1.9	08 13 39.87 ± 0.04	75 48 00.8 ± 0.2	17.5
B 0905+352	FIRST			< 0.45	09 05 41.90 ± 0.03	35 18 31.9 ± 0.4	18.0
B 0925+420	FIRST	09 25 59.72 ± 0.01	41 59 54.7 ± 0.1	6.7 ± 0.4	09 25 59.95 ± 0.01	41 59 54.2 ± 0.1	18.3
B 0935+743	NVSS	09 34 56.30 ± 0.28	74 19 02.7 ± 1.4	15.6 ± 1.2	09 34 55.66 ± 0.01	74 19 03.9 ± 0.1	14.2
B 1029+281	FIRST	10 29 26.77 ± 0.01	28 11 28.7 ± 0.1	35.4 ± 0.8	10 29 26.80 ± 0.01	28 11 27.2 ± 0.1	14.3
B 1044+745	NVSS	10 44 08.08 ± 1.24	74 35 19.8 ± 6.4	4.1 ± 1.2	10 44 04.53 ± 0.02	74 35 25.8 ± 0.1	14.0
B 1110+405	FIRST	11 10 19.90 ± 0.01	40 33 49.3 ± 0.1	10.9 ± 0.5	11 10 19.92 ± 0.01	40 33 48.1 ± 0.1	11.4
B 1144+352	FIRST	11 44 45.52 ± 0.01	35 17 47.4 ± 0.1	609.3 ± 12.2[a]	11 44 45.55 ± 0.01	35 17 46.7 ± 0.1	14.2
B 1213+422	FIRST	12 13 39.78 ± 0.01	42 16 08.2 ± 0.1	18.2 ± 0.5	12 13 39.76 ± 0.01	42 16 06.6 ± 0.1	15.9
B 1245+676	NVSS	12 45 32.12 ± 0.01	67 39 37.9 ± 0.1	269.8 ± 5.4	12 45 32.19 ± 0.01	67 39 37.1 ± 0.1	14.3
B 1306+621	WSRT	13 06 47.49 ± 0.02	62 10 14.9 ± 0.1	9.2 ± 0.5	13 06 47.66 ± 0.01	62 10 13.7 ± 0.1	16.0
B 1310+451	FIRST	13 10 03.59 ± 0.01	45 06 15.2 ± 0.1	52.8 ± 1.1	13 10 03.59 ± 0.01	45 06 15.4 ± 0.1	9.8
B 1416+380	FIRST	14 16 33.21 ± 0.01	38 00 10.3 ± 0.1	5.2 ± 0.4	14 16 33.35 ± 0.01	38 00 09.8 ± 0.1	14.5
B 1426+295	FIRST	14 26 08.03 ± 0.01	29 32 06.3 ± 0.1	12.8 ± 0.4	14 26 08.09 ± 0.01	29 32 05.8 ± 0.1	13.0
B 1450+333	FIRST	14 50 58.95 ± 0.02	33 20 55.0 ± 0.2	1.9 ± 0.2	14 50 59.03 ± 0.01	33 20 53.6 ± 0.1	18.3
B 1543+845	NVSS	15 43 55.6 ± 1.8	84 32 52.6 ± 2.5	5.8 ± 0.5	15 43 48.93 ± 0.02	84 32 44.1 ± 0.1	18.7
B 1709+464	FIRST	17 09 33.20 ± 0.01	46 27 56.5 ± 0.1	13.2 ± 0.4	17 09 33.31 ± 0.01	46 27 56.0 ± 0.1	10.4
B 1736+375	NVSS	17 36 38.03 ± 0.01	37 35 12.3 ± 0.1	119.0 ± 2.5	17 36 38.35 ± 0.01	37 35 11.7 ± 0.1	15.9
B 1852+507	NVSS	18 52 18.02 ± 0.05	50 42 22.8 ± 0.7	34.4 ± 1.4	18 52 18.36 ± 0.01	50 42 17.0 ± 0.1	12.8
B 1911+470	NVSS	19 11 50.21 ± 0.01	47 01 43.6 ± 0.1	164.9 ± 3.5	19 11 50.52 ± 0.01	47 01 36.9 ± 0.1	11.6
B 1918+516	WSRT	19 18 08.42 ± 0.01	51 37 51.4 ± 0.1	19.2 ± 0.4	19 18 08.55 ± 0.01	51 37 56.3 ± 0.1	19.2[b]
B 2147+816	NVSS	21 47 12.01 ± 0.4	81 40 58.3 ± 0.9	12.9 ± 0.9	21 47 12.30 ± 0.01	81 40 57.3 ± 0.1	16.5

Notes:

a−Variable (see Schoenmakers et al. 1999b)

b−Merged with nearby star on DSS; the magnitude has been determined by subtracting the flux from the star, obtained by fitting a Gaussian, from the integrated flux of the star and galaxy combined. The error is therefore large (estimated at 1 mag.).

Table A.4. Radio properties of the sources from Tab. A.3. Column 1 gives the source name in IAU format. Column 2 gives the integrated flux density of the source at 325 MHz from the WENSS (unless states otherwise). Column 3 gives the integrated flux density at 1400 MHz from the NVSS. Column 5 gives the spectral index between 325 and 1400 MHz. Column 6 gives the redshift of the host galaxy. Column 7 gives the angular size of the radio source in arcminute. Column 8 gives the projected linear size in Mpc. Column 9 gives the radio luminosity at an emitted frequency of 325 MHz.

(1) Source	(2) S_{325} [Jy]	(3) S_{1400} [mJy]	(4) α_{325}^{1400}	(5) z	(6) θ [′]	(7) D [Mpc]	(8) $\log(P_{325})$ [W Hz^{-1}]
B 0211+326	1.67 ± 0.04	470 ± 11	-0.87 ± 0.03	0.2605 ± 0.0002	5.2 ± 0.1	1.57 ± 0.03	26.72 ± 0.02
B 0217+367	2.70 ± 0.06	828 ± 18	-0.81 ± 0.03	0.0368 ± 0.0003	15.8 ± 0.5	0.95 ± 0.03	25.20 ± 0.02
B 0648+733	2.41 ± 0.06^a	861 ± 18^b	-0.70 ± 0.04	0.1145 ± 0.0002	12.6 ± 0.2	1.95 ± 0.04	26.14 ± 0.01
B 0648+431	0.75 ± 0.03	328 ± 7	-0.57 ± 0.04	0.0891 ± 0.0002	9.6 ± 0.5	1.28 ± 0.07	25.41 ± 0.02
B 0658+490	1.07 ± 0.04	399 ± 9	-0.68 ± 0.04	0.0650 ± 0.0002	19.1 ± 0.2	1.94 ± 0.02	25.29 ± 0.02
B 0747+426	0.62 ± 0.03^c	164 ± 6^d	-0.91 ± 0.06	0.2030 ± 0.0004	6.0 ± 0.5	1.54 ± 0.13	26.06 ± 0.03
B 0750+434	0.29 ± 0.02	124 ± 4	-0.58 ± 0.07	0.3474 ± 0.0003	8.1 ± 0.1	2.90 ± 0.04	26.19 ± 0.03
B 0757+477	0.29 ± 0.02	160 ± 3	-0.41 ± 0.06	0.1567 ± 0.0002	6.0 ± 0.3	1.27 ± 0.06	25.48 ± 0.03
B 0801+741	0.62 ± 0.04	150 ± 4	-0.97 ± 0.06	0.1204 ± 0.0002	6.3 ± 0.2	1.08 ± 0.05	25.61 ± 0.03
B 0809+454	0.30 ± 0.02	125 ± 4	-0.60 ± 0.06	0.2204 ± 0.0003	6.9 ± 0.1	1.87 ± 0.03	25.80 ± 0.03
B 0813+758	2.14 ± 0.05^c	621 ± 13	-0.89 ± 0.03	0.2324 ± 0.0003	8.3 ± 0.2	2.33 ± 0.06	26.71 ± 0.01
B 0905+352	0.59 ± 0.02	200 ± 5	-0.74 ± 0.04	0.106 ± 0.001	6.3 ± 0.1	0.98 ± 0.02	25.47 ± 0.02
				0.260 ± 0.002		1.90 ± 0.03	26.26 ± 0.02
B 0925+420^e	0.55 ± 0.02	169 ± 4	-0.81 ± 0.04	0.365 ± 0.005	6.6 ± 0.2	2.43 ± 0.07	26.54 ± 0.02
B 0935+743	0.19 ± 0.03	94 ± 2	-0.48 ± 0.11	0.1215 ± 0.0003	7.3 ± 0.3	1.27 ± 0.05	25.08 ± 0.04
B 1029+281	0.65 ± 0.05^f	295 ± 7^f	-0.54 ± 0.07	0.0854 ± 0.0002	11.0 ± 0.3	1.42 ± 0.04	25.31 ± 0.03
B 1044+745	0.12 ± 0.06^g	85 ± 5	-0.3 ± 0.3	0.1210 ± 0.0003	11.2 ± 0.3	1.93 ± 0.05	24.9 ± 0.2
B 1110+405	0.79 ± 0.04^h	246 ± 6	-0.80 ± 0.05	0.0745 ± 0.0003	12.0 ± 1.0	1.37 ± 0.11	25.28 ± 0.03
B 1144+352^i	0.89 ± 0.06	805 ± 18	-0.07 ± 0.06	$0.063^j \pm 0.001$	11.8 ± 0.1	1.17 ± 0.01	25.17 ± 0.03
B 1213+422	1.19 ± 0.03	419 ± 9	-0.71 ± 0.03	0.2426 ± 0.0002	5.2 ± 0.1	1.50 ± 0.03	26.50 ± 0.01
B 1245+676	0.26 ± 0.03	386 ± 9	$+0.27 \pm 0.10$	$0.1073^k \pm 0.0001$	11.6 ± 0.2	1.82 ± 0.03	25.07 ± 0.05
B 1306+621	0.24 ± 0.02	101 ± 4	-0.59 ± 0.09	0.1625 ± 0.0004	8.9 ± 0.1	1.94 ± 0.02	25.44 ± 0.04
B 1310+451	0.72 ± 0.04	305 ± 8	-0.59 ± 0.05	0.0358 ± 0.0002	22.6 ± 0.5	1.33 ± 0.03	24.60 ± 0.03
B 1416+380	0.49 ± 0.02	58 ± 3	-1.46 ± 0.03	0.1350 ± 0.0002	7.4 ± 0.5	1.40 ± 0.09	25.64 ± 0.02
B 1426+295	1.15 ± 0.04	431 ± 10	-0.67 ± 0.04	0.0870 ± 0.0003	14.7 ± 0.4	1.92 ± 0.05	25.58 ± 0.02
B 1450+333^e	1.51 ± 0.04	460 ± 10	-0.81 ± 0.04	0.249 ± 0.001	5.7 ± 0.1	1.68 ± 0.03	26.63 ± 0.01
B 1543+845	1.14 ± 0.03^g	378 ± 8	-0.80 ± 0.03	0.201 ± 0.001	7.9 ± 0.3	2.03 ± 0.07	26.35 ± 0.01
B 1709+464	1.30 ± 0.04	461 ± 10	-0.71 ± 0.04	0.0368 ± 0.0002	9.8 ± 0.3	0.59 ± 0.02	24.88 ± 0.02
B 1736+375	0.51 ± 0.02	237 ± 5	-0.52 ± 0.04	0.1562 ± 0.0003	6.5 ± 0.3	1.37 ± 0.06	25.73 ± 0.02
B 1852+507	0.30 ± 0.02	131 ± 4	-0.57 ± 0.06	0.0958 ± 0.0003	7.0 ± 0.3	1.00 ± 0.04	25.08 ± 0.03
B 1911+470	0.87 ± 0.03	341 ± 4	-0.64 ± 0.03	0.0548 ± 0.0002	6.2 ± 0.3	0.54 ± 0.03	25.05 ± 0.02
B 1918+516	1.20 ± 0.03^l	363 ± 9^m	-0.82 ± 0.03	0.284 ± 0.001^n	7.3 ± 0.1	2.32 ± 0.03	26.65 ± 0.01
B 2147+816	1.06 ± 0.05^g	414 ± 10	-0.68 ± 0.05	0.1457 ± 0.0001	18.3 ± 0.2	3.66 ± 0.04	26.00 ± 0.02

Notes:
$a-$Subtracted 41 ± 7 mJy background object at R.A. 06 49 02.7, Dec. 73 25 55.
$b-$Subtracted 19.8 ± 1.1 mJy background object at R.A. 06 49 02.7, Dec. 73 25 55.
$c-$Subtracted 149 ± 11 mJy background object at R.A. 07 47 48.2, Dec. 42 39 56.
$d-$Subtracted 26 ± 1 mJy background object at R.A. 07 47 48.2, Dec. 42 39 56.
$e-$See Schoenmakers et al. (2000a) for radio maps and optical spectrum of this source.
$f-$Includes background source at R.A. 10 29 36.3 Dec. 28 13 15.9 (flux density 10 ± 1 mJy at 1400 MHz).
$g-$WENSS polar cap region (observed frequency 351 MHz).
$h-$Subtracted 72 ± 7 mJy background object at R.A. 11 10 24.8, Dec. 40 38 03.
$i-$See Schoenmakers et al. (1999b) for radio maps and optical spectrum of this source.
$j-$Colla et al. (1975).
$k-$Marcha et al. (1996).
$l-$Subtracted 90 ± 7 mJy background source at R.A. 19 18 17.1, Dec. 51 37 53.
$m-$Subtracted 26 ± 1 mJy background source at R.A. 19 18 17.1, Dec. 51 37 53.
$n-$Uncertain redshift.

Table A.5. The measured wavelengths and resulting redshifts of the most prominent emission and absorption lines. Column 1 gives the name of the source, column 2 the used line, column 3 the measured wavelength, i.e. the position of the peak of the Gaussian used in fitting the line, and column 4 the therefrom derived redshift of that line. The last line for each source gives the average redshift.

(1) Source	(2) Line	(3) $\lambda_{\rm peak}$/[Å]	(4) Redshift
B 0211+326	[OII]3727	4697.04	0.2603
	[NeIII]	4877.16	0.2606
	Hβ	6127.18	0.2605
	[OIII]4959	6250.79	0.2605
	[OIII]5007	6311.32	0.2605
			0.2605 ± 0.0002
B 0217+367	CaII3934	4078.60	0.0368
	CaII3968	4115.06	0.0371
	G-band	4462.41	0.0366
	Mg-b	5364.99	0.0367
	Na D	6110.44	0.0369
			0.0368 ± 0.0003
B 0648+733	G-band	4798.18	0.1146
	Hβ	5417.93	0.1146
	[OIII]4959	5527.37	0.1146
	[OIII]5007	5580.97	0.1146
	Mg-b	5766.97	0.1144
	[OI]6300	7020.84	0.1144
	[NII]6583	7336.42	0.1144
			0.1145 ± 0.0002
B 0648+431	G-band	4688.06	0.0890
	Mg-b	5636.05	0.0891
	Na D	6418.92	0.0892
			0.0891 ± 0.0002
B 0658+490	Mg-b	5511.23	0.0650
	Na D	6275.81	0.0650
	[NII]6583	7010.76	0.0650
			0.0650 ± 0.0002
B 0747+426[a]	[OII]3727	4483.93	0.2031
	CaII3934	4731.23	0.2027
	CaII3968	4772.31	0.2027
	G-band	5178.74	0.2030
	Mg-b	6228.69	0.2036
			0.2030 ± 0.0004
B 0750+434	[NeV]3426	4615.94	0.3473
	[OII]3727	5022.40	0.3476
	[NeIII]3869	5211.82	0.3471
	[OIII]4363	5879.17	0.3475
	Hβ	6550.15	0.3475
	[OIII]4959	6681.97	0.3474
	[OIII]5007	6746.39	0.3474
			0.3474 ± 0.0003
B 0757+472	Hγ	5019.76	0.1566
	Hβ	5622.10	0.1566
	[OIII]4959	5736.78	0.1568
	[OIII]5007	5792.23	0.1568
			0.1567 ± 0.0002
B 0801+741	Hβ	5446.74	0.1205
	[OIII]5007	5610.22	0.1205
	Na D	6603.31	0.1205
	[OI]6300	7058.78	0.1204
	Hα	7351.97	0.1202
	[SII]6583	7524.50	0.1204
			0.1204 ± 0.0002
B 0809+454	[OII]3727	4548.56	0.2204
	Hβ	5933.56	0.2206
	[OIII]4959	6052.08	0.2204
	[OIII]5007	6109.84	0.2203
	Hα	8007.07	0.2200
			0.2204 ± 0.0003
B 0813+758	[OII]3727	4591.00	0.2318
	Hβ	5989.61	0.2322
	[OIII]4959	6111.66	0.2324
	[OIII]5007	6170.54	0.2324
	[OI]6300	7766.57	0.2328
	Hα	8089.26	0.2326
			0.2324 ± 0.0003
B 0905+352	[NII]6548	7242.29	0.1059
	[NII]6583	7279.51	0.1058
			0.106 ± 0.001
or			
	G-band	5422.53	0.2596
	Mg-b	6512.59	0.2585
			0.260 ± 0.002
B 0935+743	CaII3968	4448.92	0.1212
	Mg-b	5806.05	0.1219
	Na D	6608.56	0.1214
			0.1215 ± 0.0003
B 1029+281	Hβ	5274.68	0.0851
	[OIII]4959	5382.18	0.0853
	[OIII]5007	5434.69	0.0854
	Mg-b	5618.53	0.0857
	Na D	6397.44	0.0856
	[OI]6300	6837.35	0.0853
	Hα	7121.47	0.0851
			0.0854 ± 0.0002
B 1044+745[a]	CaII3968	4448.36	0.1211
	Mg-b	5800.85	0.1209
	Na D	6606.56	0.1211
			0.1210 ± 0.0003

Continued on next page...

...Continued from previous page

(1) Source	(2) Line	(3) $\lambda_{\rm peak}$/[Å]	(4) Redshift
B 1110+405	G-band	4625.03	0.0743
	Na D	6332.42	0.0746
	[NII]6583	7073.81	0.0746
			0.0745 ± 0.0003
B 1213+422	[OII]3727	4632.22	0.2429
	[NeIII]3869	4806.84	0.2424
	[OIII]4363	5422.13	0.2428
	Hβ	6041.38	0.2428
	[OIII]4959	6162.09	0.2426
	[OIII]5007	6221.83	0.2426
	[OI]6300	7828.06	0.2425
	Hα	8154.30	0.2425
			0.2426 ± 0.0002
B 1306+621[a]	CaII3934	4574.07	0.1627
	CaII3968	4612.79	0.1625
	G-band	5003.63	0.1623
	Mg-b	6016.99	0.1627
			0.1625 ± 0.0004
B 1310+451	CaII3934	4075.03	0.0358
	CaII3968	4110.96	0.0360
	G-band	4458.96	0.0358
	Mg-b	5359.83	0.0357
	Na D	6102.51	0.0356
	[NII]6583	6817.81	0.0357
			0.0358 ± 0.0002
B 1416+380	Mg-b	5874.33	0.1351
	Na D	6688.00	0.1349
	[OI]6300	7150.68	0.1350
	Hα	7448.93	0.1350
	[NII]6583	7471.70	0.1350
			0.1350 ± 0.0002
B 1426+295	G-band	4678.63	0.0868
	[OIII]4363	4742.83	0.0871
	Hβ	5283.63	0.0869
	Mg-b	5627.45	0.0874
	Na D	6403.01	0.0865
	[NII]6583	7156.50	0.0871
			0.0870 ± 0.0003
B 1543+845[a]	[OIII]4959	5955.22	0.2009
	[OIII]5007	6013.78	0.2011
			0.201 ± 0.001
B 1709+464	CaII3968	4114.19	0.0368
	G-band	4463.67	0.0369
	Mg-b	5366.13	0.0369
	Na D	6108.30	0.0365
	[NII]6583	6824.31	0.0367
			0.0368 ± 0.0002
B 1736+375	CaII3968	4548.75	0.1563
	Mg-b	5984.90	0.1565
	Na D	6811.76	0.1559
			0.1562 ± 0.0003
B 1852+507	G-band	4717.29	0.0958
	Mg-b	5670.70	0.0958
	Na D	6457.09	0.0957
			0.0958 ± 0.0003
B 1911+470	G-band	4540.16	0.0546
	Mg-b	5457.87	0.0547
	Na D	6216.32	0.0549
	[NII]6583	6944.73	0.0549
			0.0548 ± 0.0002
B 1918+512	CaII3968	5050.42	0.2838
	[OIII]5007	6425.44	0.2833
			0.284 ± 0.001
B 2147+816	[OII]3727	4270.15	0.1457
	[NeIII]3869	4432.08	0.1455
	Hγ	4972.15	0.1457
	[OIII]4363	4998.67	0.1457
	Hβ	5568.67	0.1456
	[OIII]4959	5681.59	0.1457
	[OIII]5007	5736.42	0.1457
			0.1457 ± 0.0001

Notes:
$a-$Spectrum has been smoothed with a 3 pixel rectangular box.

Table A.6. The flux density levels of the first contour in the presented radio contour maps. Column 1 gives the name of the source; columns 2 to 5 give the flux density of the first contour in the radio contour plots of the WENSS, NVSS, FIRST and WSRT radio map. Column 6 gives the beam size of the WSRT beam in cases where a WSRT radio map is presented. Column 7 gives the origin of the presented optical images. Here, PI stands for POSS-I, PII for POSS-II; LDSS is an imaging spectrograph on the 4.2-m WHT on La Palma, HARIS is an imaging spectrograph on the 2.2-m University of Hawaii telescope on Mauna Kea. Unless indicated otherwise, contour levels have been plotted at $-1, 1, 2, 4, 8, 16, 32, 64, 128, 256$ times the flux density level presented in this table.

(1) Source	(2) WENSS	(3) NVSS	(4) FIRST	(5) WSRT	(6) Beam size	(7) Optical
	[mJy beam^{-1}]				[$'' \times ''$]	
B 0211+326	8			2.5	26.11×12.56	PII
B 0217+367	8	1.2		1.2	20.85×12.65	PII
B 0648+733	10	1.3		0.8	17.06×11.18	PI
B 0648+431	8	1.3		0.8	20.85×12.65	PII
B 0658+490	8	1.3	0.55			PII
B 0747+426	8	1.5	0.45			PII
B 0750+434	8	1.3	0.45			PII
B 0757+477	10	1.3	0.45			PII
B 0801+741	11	1.3		0.8	16.39×11.30	PII
B 0809+454	10	1.3	0.45			PII
B 0813+758	8	1.3		1.5	21.80×9.70	PII
B 0905+352	8		0.45			PI
B 0935+743	10	1.2				PII
B 1029+281	18	1.2	0.55			PII
B 1044+745	7[a]	1.2[a]				PI
B 1110+405	8	1.3	0.70			PII
B 1213+422	8		0.45			PII
B 1245+676	8	1.2				PI
B 1306+621	8	1.2		0.5	16.63×12.79	PI
B 1310+451	8	1.3	0.50			PI
B 1416+380	8	1.3	0.45			PII
B 1426+295	12	1.5	0.60			PII
B 1543+845	7	1.3				HARIS
B 1709+464	10	1.3	0.45			PII
B 1736+375	8	1.3				PI
B 1852+507	8	1.3				PII
B 1911+470	8	1.3				PII
B 1918+516	8			0.5	16.22×12.25	LDSS
B 2147+816	5	1.3				PII

Notes:
$a-$Extra contour plotted at a level of $\sqrt{2}$ times the lowest contour level.

Fig. A.1. B 0211+326: The WENSS radio contour plot, an overlay of the WSRT radio map (contours) with an optical image (grey scale; the identification has been encircled) and the optical spectrum of the host galaxy.

Fig. A.2. B 0217+367: The WENSS (upper) and NVSS (lower) radio contour plots, an overlay of the WSRT radio map (contours) with an optical image (grey scale) and the optical spectrum of the host galaxy.

Fig. A.3. B 0648+733: The WENSS (left) and NVSS (right) radio contour plots, an overlay of the WSRT radio map (contours) with an optical image (grey scale) and the optical spectrum of the host galaxy.

Fig. A.4. B 0648+431: The WENSS (upper) and NVSS (lower) radio contour plots, an overlay of the WSRT radio map (contours) with an optical image (grey scale) and the optical spectrum of the host galaxy.

Fig. A.5. B 0658+490: The WENSS (upper) and NVSS (lower) radio contour plots, an overlay of the WSRT radio map (contours) with an optical image (grey scale) and the optical spectrum of the host galaxy.

Fig. A.6. B 0747+426: The WENSS (upper) and NVSS (lower) radio contour plots, an overlay of the FIRST radio map (contours) with an optical image (grey scale; the identification has been encircled) and the optical spectrum of the host galaxy.

Fig. A.7. B 0750+434: The WENSS (upper) and NVSS (lower) radio contour plots, an overlay of the FIRST radio map (contours) with an optical image (grey scale) and the optical spectrum of the host galaxy.

Fig. A.8. B 0757+477: The WENSS (upper) and NVSS (lower) radio contour plots, an overlay of the FIRST radio map (contours) with an optical image (grey scale) and the optical spectrum of the host galaxy.

Fig. A.9. B 0801+741: The WENSS (upper) and NVSS (lower) radio contour plots, an overlay of the WSRT radio map (contours) with an optical image (grey scale) and the optical spectrum of the host galaxy.

Fig. A.10. B 0809+454: The WENSS (upper) and NVSS (lower) radio contour plots, an overlay of the FIRST radio map (contours) with an optical image (grey scale) and the optical spectrum of the host galaxy.

Fig. A.11. B 0813+758: The WENSS (upper) and NVSS (lower) radio contour plots, an overlay of the WSRT radio map (contours) with an optical image (grey scale) and the optical spectrum of the host galaxy.

Fig. A.12. B 0905+352: The WENSS radio contour plot, an overlay of the FIRST radio map (contours) with an optical image (grey scale; the identification has been encircled) and the optical spectrum of the host galaxy.

Fig. A.13. B 0935+352: The WENSS radio contour plot, an overlay of the NVSS radio map (contours) with an optical image (grey scale) and the optical spectrum of the host galaxy.

Fig. A.14. B 1029+281: The WENSS (upper) and NVSS (lower) radio contour plots, an overlay of the FIRST radio map (contours) with an optical image (grey scale) and the optical spectrum of the host galaxy.

Fig. A.15. B 1044+745: The WENSS radio contour plot, an overlay of the NVSS radio map (contours) with an optical image (grey scale) and the optical spectrum of the host galaxy.

Fig. A.16. B 1110+405: The WENSS (upper) and NVSS (lower) radio contour plots, an overlay of the FIRST radio map (contours) with an optical image (grey scale) and the optical spectrum of the host galaxy.

Fig. A.17. B 1213+422: The WENSS radio contour plot, an overlay of the FIRST radio map (contours) with an optical image (grey scale) and the optical spectrum of the host galaxy.

Fig. A.18. B 1245+676: The WENSS radio contour plot and an overlay of the NVSS radio map (contours) with an optical image (grey scale). An optical spectrum has been published by Marcha et al. (1996).

Fig. A.19. B 1306+621: The WENSS (left) and NVSS (right) radio contour plots, an overlay of the WSRT radio map (contours) with an optical image (grey scale) and the optical spectrum of the host galaxy.

Fig. A.20. B 1310+451: The WENSS (upper) and NVSS (lower) radio contour plots, an overlay of the FIRST radio map (contours) with an optical image (grey scale) and the optical spectrum of the host galaxy.

Fig. A.21. B 1416+380: The WENSS (upper) and NVSS (lower) radio contour plots, an overlay of the FIRST radio map (contours) with an optical image (grey scale) and the optical spectrum of the host galaxy.

Fig. A.22. B 1426+295: The WENSS (left) and NVSS (right) radio contour plots, an overlay of the FIRST radio map (contours) with an optical image (grey scale) and the optical spectrum of the host galaxy.

Fig. A.23. B 1543+845: The WENSS (upper) and NVSS (lower) radio contour plots, an overlay of the NVSS radio map (contours) with an optical image (grey scale) and the optical spectrum of the host galaxy.

Fig. A.24. B 1709+464: The WENSS (upper) and NVSS (lower) radio contour plots, an overlay of the FIRST radio map (contours) with an optical image (grey scale) and the optical spectrum of the host galaxy.

Fig. A.25. B 1736+375: The WENSS radio contour plot, an overlay of the NVSS radio map (contours) with an optical image (grey scale) and the optical spectrum of the host galaxy of the central source; note the fuzzy optical object near the center of the northern radio component.

Fig. A.26. B 1852+507: The WENSS radio contour plot, an overlay of the NVSS radio map (contours) with an optical image (grey scale) and the optical spectrum of the host galaxy.

Fig. A.27. B 1911+470: The WENSS radio contour plot, an overlay of the NVSS radio map (contours) with an optical image (grey scale) and the optical spectrum of the host galaxy.

Fig. A.28. B 1918+516: The WENSS radio contour plot, an overlay of the 1.4-GHz WSRT radio map (contours) with an optical image (grey scale; the identification is indicated by the arrow) and the optical spectrum of the host galaxy.

Fig. A.29. B 2147+816: The WENSS (upper) and NVSS (lower) radio contour plots, an overlay of the NVSS radio map (contours) with an optical image (grey scale) and the optical spectrum of the host galaxy.